TECHNISCHE UNIVERSITÄT DRESDEN

Fakultät Maschinenwesen, Professur für Transportprozesse an Grenzflächen

Diplomarbeit

Numerical simulation of radial A+B → C reaction fronts

Bearbeiter	**Daniel Fischer**
geboren am	11. Januar 1997
in	Köln
Eingereicht am	30.01.2023
Betreuender Hochschullehrer	Prof. Dr. rer. nat. et Ing. habil. Kerstin Eckert
Betreuer	Dr.-Ing. Karin Schwarzenberger
	Dipl.-Ing. Yorgos Stergiou

TECHNISCHE UNIVERSITÄT DRESDEN

Fak. Maschinenwesen Inst. Verfahrenstechnik u. Umwelttechnik, Prof. Transportprozesse an Grenzflächen

Aufgabenstellung für die Diplomarbeit

im Studiengang:	Verfahrenstechnik und Naturstofftechnik
in der Studienrichtung:	Chemieingenieurtechnik
Name des Studenten:	Daniel F i s c h e r
Matrikelnummer:	4517353

Thema: **Numerical simulations of radial A + B → C reaction fronts**

A + B → C reaction fronts can describe various natural or technological systems that combine specific dynamics, namely: Reaction, Diffusion and Advection (RDA). In this context, the study of the simple A + B → C reaction in a circular geometry, where reactant solution A is injected radially into solution B at a constant flowrate in a vertically confined system, provides valuable data for a variety of technological applications such as in microfluidics or in reactive mass transfer in porous media. This work consists of a two-dimensional numerical study of such fronts and aims to add to the existing knowledge by providing insights of the early-time regime, for which experimental outreach is not possible. Various temporal metrics are analyzed, such as the front position, the production rate and the front width. Adjusting geometrical, flow or physical property parameters, the effect on reaction and mass transfer can be studied to enhance understanding of the dynamics present in such fronts in early times and their contribution in shaping the front for later-time stages.

Task description:

- Literature research on radial A+B → C reaction fronts and their technological applications.
- Setup of the two-dimensional numerical simulations: mesh design, calculation methods, post-processing, parallel computing.
- Mesh dependency study and validation of the numerical code with the use of preexisting experimental results.
- Rendering of detailed 2D-views of early-time reaction fronts, otherwise non-accessible through experiments.
- Variation of flow field geometry.
- Parametric study of the front's response to changes in the flow conditions and the fluid properties.
- Comprehensive discussion of the results regarding the product formation rate, the front width and other relevant reaction front metrics in radial reactors.
- Discussion of current limitations and future directions of the work.

Die von der Studienrichtung erlassenen Richtlinien zur Anfertigung der Diplomarbeit sowie die Prüfungsordnung sind zu beachten.

Betreuer: Dipl.-Ing. Yorgos Stergiou, HZDR
Dr.-Ing. Karin Schwarzenberger, IVU, TU Dresden

Ausgabe: 31.08.2022
Abgabe: 30.01.2023

Michael Stintz
Digital unterschrieben von Michael Stintz
DN: c=DE, o=Technische Universitaet Dresden, cn=Michael Stintz
Datum: 2022.10.07 17:24:10 +02'00'

Prof. Dr.-Ing. habil. Michael Stintz
Studienrichtungsleiter

Kerstin Eckert
Digital unterschrieben von Kerstin Eckert
DN: c=DE, o=Technische Universitaet Dresden, cn=Kerstin Eckert
Datum: 2022.10.10 13:06:20 +02'00'

Prof. Dr. et Ing. habil. Kerstin Eckert
Betreuende Hochschullehrerin

Contents

Abstract

Within this work a parametric study investigating the influence of different parameters on an evolving Reaction-Diffusion-Advection front within a radial reactor is performed. A numerical model is created and implemented in `ANSYS FLUENT`. The model validation is done using existing experimental data. After assuring that the model shows physically believable behaviour, a parameter study is done using the dimensionless variables Pe and Sc. The investigated variables are the front position, the fronts width and the total amount of product formed. These variables show a different behaviour, dependant on the reactor's geometry and input variable values.

In dieser Arbeit wird der Einfluss einiger Eingangsgrößen auf eine sich bildende Reaction-Diffusion-Advection Front in einem zylindrischen Reaktor untersucht. Ein numerisches Modell wird dazu erstellt und in der Software `ANSYS FLUENT` implementiert. Das entwickelte Modell wird mit bestehenden experimentellen Daten verglichen, um eine korrekte Funktionsweise zu gewährleisten. Anschließend wird eine Parameter Studie anhand der dimensionslosen Kennzahlen Pe und Sc durchgeführt. Es wird der Einfluss dieser Parameter auf die Position der Reaktionsfront, sowie die Breite der Front, als auch das insgesamt gebildete Produkt beschrieben und erklärt. Das Verhalten dieser Ausgangsgrößen zeigt eine starke Abhängigkeit von der Reaktor Geometrie, sowie der veränderten Eingangsgrößen.

List of Symbols

latin symbols	**unit**	**meaning**
Sc	-	Schmidt number
Pe	-	Peclet number
c	-	Courant number
t	s	time
p	Pa	pressure
T	K	temperature
R	$\frac{\mathrm{J}}{\mathrm{mol \cdot K}}$	gas constant
u	$\frac{\mathrm{m}}{\mathrm{s}}$	velocity
U	$\frac{\mathrm{m}}{\mathrm{s}}$	gap averaged velocity
D	$\frac{\mathrm{m}^2}{s}$	diffusion coefficient
D_{eff}	$\frac{\mathrm{m}^2}{s}$	effective diffusion coefficient
M_i	$\frac{\mathrm{g}}{\mathrm{mol}}$	molar mass of species i
m	$\frac{\mathrm{mol}}{\mathrm{s}}$	production rate
E_A	$\frac{\mathrm{J}}{\mathrm{mol}}$	activation energy
k_∞	$\frac{\mathrm{l}^2}{\mathrm{mol \cdot s}}$	pre-exponential factor
k	$\frac{\mathrm{l}^2}{\mathrm{mol \cdot s}}$	rate constant
r	$\frac{\mathrm{mol}}{\mathrm{s}}$	reaction rate
r_{max}	mm	radial position of reaction front's maximum
r_{front}	mm	radial position of reaction front's front position
x_i	-	mole fraction of species i
φ_i	-	mass fraction of species i

greek symbols	**unit**	**meaning**
α	-	non-dimensional helmholtz energy
ρ	$\frac{\mathrm{kg}}{\mathrm{m}^3}$	density
ν	$\frac{\mathrm{m}^2}{s}$	viscosity
$\nu_{i,r}$	-	stoichiometric number for species i
$\eta_{j,r}$	-	rate exponent of species j
σ	-	geometric factor

abbreviation	**meaning**
RDA	reaction-diffusion-advection
PDE	partial differential equation
CFD	computational fluid dynamics
PISO	pressure implicit with splitting operation
QUICK	Quadratic upstream interpolation for convective kinetics
FWHM	Full Width at Half Maximum
FWHMHGH	Full Width at Half Maximum at Half Gap Height
VOF	Volume of Fluid

List of Figures

List of Tables

1. Introduction

This chapter gives a short introduction to the overall research field this work addresses. After that is done the objectives and structure of this work are explained.

1.1. Motivation

With the development towards higher resource efficiency and sustainability, new materials and chemicals have to be developed to replace the fossil based ones currently in use today. With the demand of materials constantly changing and new developments needing scale-up from laboratory scale to industrial scale, the research in microfluidic reactors has gained more and more significance in recent history. These systems have the advantage of being easily customizable and having the capability of dealing with toxic or explosive materials, due to their low reaction volume. This, in addition to their easy to handle geometric dimensions, makes them great for laboratory research. When looking into such small reaction systems, the evolution of a reactions appearance in space and time is of high interest. Having a deeper knowledge can be used to further improve the reactions yield or heat transfer, in case of needed heating or cooling. An example of such an microfluidic system is shown in Figure 1.1. Customization being not

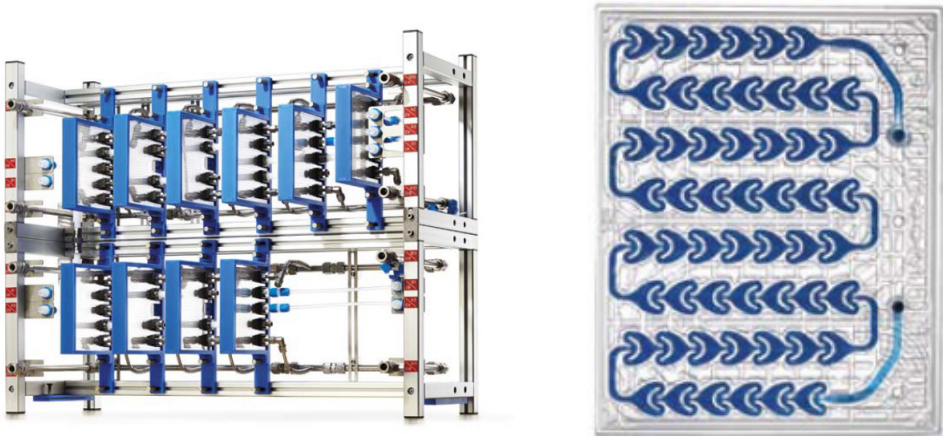

(a) micro fluidic reactor (b) micro flow element

Figure 1.1.: Microfluidic system [1]

challenging by placing different micro flow elements in series, the industry can quickly adapt to upcoming new research or changing market environments.
Reactions taking place under these conditions are affected by advection as a result of the moving fluid and diffusion as a result of concentration gradients. Therefore the whole moving system is called Reaction-Diffusion-Advection front or RDA.
Reaction-diffusion (RD) fronts do play a role in a large variety of natural and technical systems. From population dynamics [4, 5], disease spreading [6–8], biological applications like pattern formation [9], stability analysis in physics [10] to finance modelling in economics [11] and language depth modelling in linguistics [12], the RD dynamics can be applied to varies different research fields. In addition to the fields already mentioned, RD with added species transport by advection, can be used to describe their distribution within different kind of reactors in the field of chemical engineering [13] or chemistry [14, 15]. Reaction diffusion advection fronts (RDA) can also be applied to mineralization processes [16], reactions taking place within a droplet [17] or other geological processes [18] to name a few.
The foundation of reaction-diffusion-advection front research was way laid by Gálfi and Rácz [19], with their theoretical study on a one-dimensional (1D) case. Their predictions were then approved by simulations [20] and experimental observations [21] in the following years. In recent times the influence of gravitation [22] among other influences is of research interest. Theoretical and experimental studies which were mostly done for 2D rectilinear cases [13] were then carried out to radial geometries [2,23,24] and evolving surfaces [25] in more recent years. The investigations done within radial geometries for axisymmetric cases [23, 24] do focus on the long term evolutions of the fronts shape and metrics. At these later stages the front has reached a final state where it's parameters do not change any more [13].
To gain further knowledge on how the front's shapes are initially built and how the front's metrics behave at early time stages, theoretical models are needed. These models do provide a side view, otherwise not accessible by experiments with their top down point of view. As known from previous research the fronts curvature is dependent on the system's geometry and other input values. An example of such a front appearance is shown in Figure 1.2.
Within this work a model for the reaction-diffusion-advection system following the reaction $A + B \rightarrow C$ is developed for a cylindrical geometry. Within this model the two initially separated species A and B are transported through advection and diffusion. A is injected radially into B from the cylinders centreline. With these conditions set, the

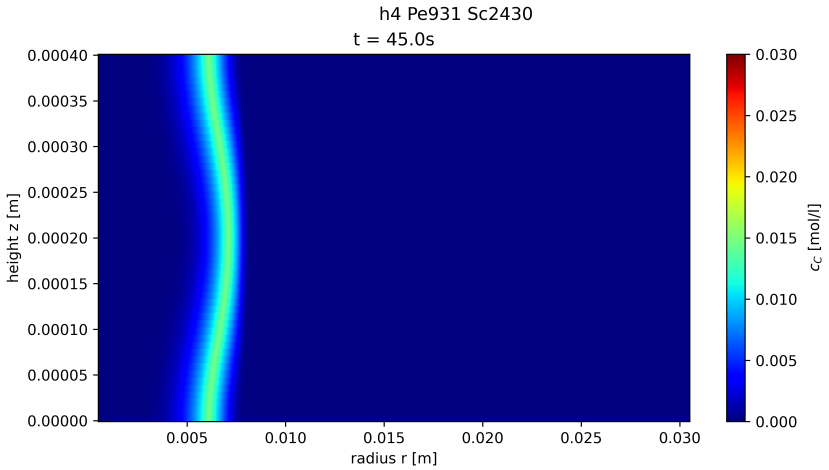

Figure 1.2.: Reaction-diffusion-advection front example

geometry does not need to be modelled in 3D, as it is assumed to be an axisymmetric problem. Therefore a 2D approach is used.
Special interest is in the species distribution at early stages of the developing reaction front. Experiments under $0g$ conditions [2] have shown that gravity affects the front's shape. These effects can be seen within the schematic in Figure 1.3. Within a model

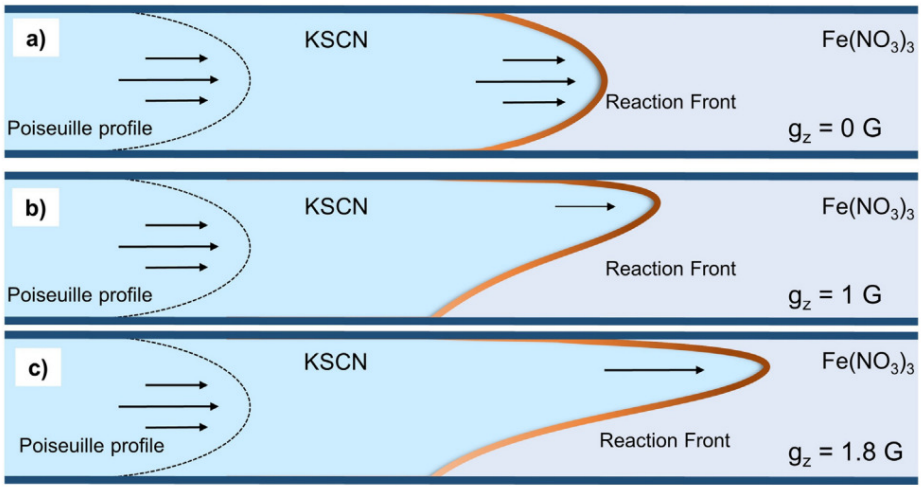

Figure 1.3.: Schematic of gravity effects on reaction fronts [2]

gravity can be turned off, so investigations by changing geometric dimensions and other input values can be done more easily and quickly.

1.2. Objectives and Report Outline

This work aims to provide detailed insights into the early-time regime within a RDA front's development process within a radial reactor, using different input parameters. To achieve that a numerical model is created using the modelling environment `ANSYS FLUENT` [26].

This work is divided into 6 chapters. The theoretical background required for modelling is given in Chapter 2. Following that the process of model creation and validation are described in Chapter 3. After that results of the parametric studies are shown and discussed within Chapter 4. Section 5 discusses the limitations of the build model. Finally Chapter 6 summarizes the work and provides an outlook for further studies.

2. Theory

Within this chapter the theory and procedures needed to solve this numerical problem are shown. At first, a broad overview is given and the generic equations are laid out. Following that is the explanation of the solution method and algorithm used in this work. After that some generic observations are explained and more details are given for the reaction. At the end of this chapter the dimensionless variables, used for the parametric study, are introduced.
Building a theoretical model describing the evolution of a reaction's species in time and space, equations that are dependent of the special coordinates and time are needed. These equations should describe the flow field and species distribution in addition to other fluid flow related quantities. These equations have the characteristic of forming a partial differential equation (PDE) system for which no analytical solution can be computed. Solving these equations numerically has lead to the development of special approaches and solution techniques. All these methods are classified under the field of Computational Fluid Dynamics or CFD in short. The basic principles of this field are explained in Section 2.1.

2.1. Computational Fluid Dynamics

Computational fluid dynamics is the computer based solving of problems regarding fluid flow, heat transfer, chemical reactions or other transport phenomena. The concept is used in a large variety of applications within the fields of engineering and science for at least 60 years [27]. Within Figure 2.1 the general procedure of solving a CFD case is shown.
The first step is to model the domains geometry. In case of `ANSYS FLUENT` this step can either be done within the CFD software itself, or an external CAD program.
The tool `ANSYS FLUENT` uses the Volume of Fluid (VOF) approach to solve fluid flow problems [26]. The theory behind this method is explained in Section 2.3. This method is based around dividing the whole volume into small elements and solving the equations for each element at a time. That is why a mesh needs to be created, to provide `ANSYS FLUENT` with the element sizes, shapes and positions in space. After the geometry is created or imported form an external source, a mesh needs to be created. This mesh is

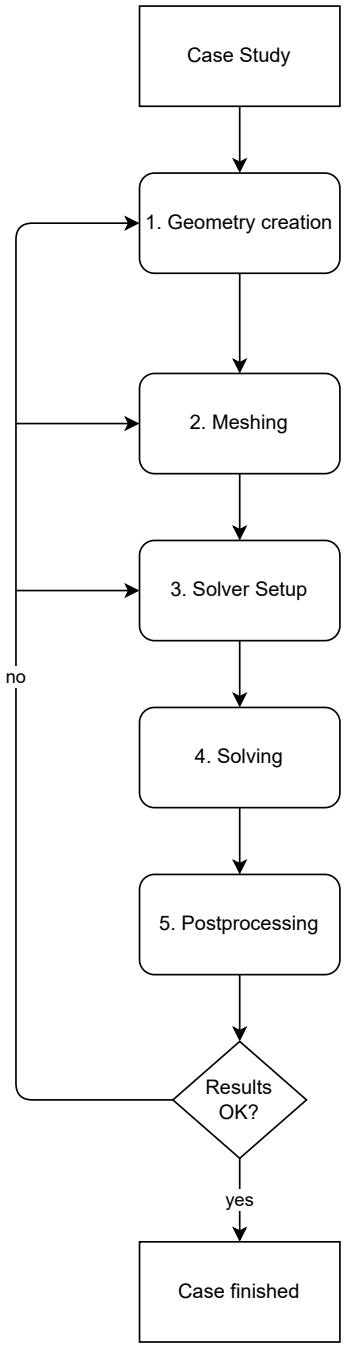

Figure 2.1.: General procedure overview for solving a CFD case

the basis for the solver to solve the case and an important step. The way the mesh is set up has a significant influence on the model's results and the computational resources needed. The finer the mesh the more computational power is needed for calculating the solution. By lowering the grid's element size the resources needed or simulation time could increase exponentially, because the amount of elements to solve growths and in addition to that, the time step to resolve all flow details might decrease as well. These two effects, that might both need to be taken into account, lead to the potential exponential growth in resources and/or simulation run time.
When meshing is finished, the next step is the solver setup. Setting up the governing equations, simulation time and boundary conditions are tasks performed in this step. The setup is described in greater detail within Section 3.1.3. After the solver is set up, the case can be run by starting the solver. Depending on the resources needed or available, this step needs some further configuration.
When the solving process has finished, the obtained results can be inspected. How these steps are performed and what steps are taken to receive the final model, are described in greater detail in Section 3.2.
All in all, solving a CFD case is an iterative process, that needs to be gone through multiple times. Validation against experimental data is important, to prove that the model shows valid behaviour and results. Further details on how these steps are performed while developing this specific model are given in Chapter 3.

2.2. Governing Equations

To obtain the results of interest the model needs to mainly solve a PDE system of three different equations. These equations are:

- mass conservation equation
- energy equation
- reaction equation
- species transfer advection-diffusion equations

In Figure 2.2 the used coordinate system is shown.

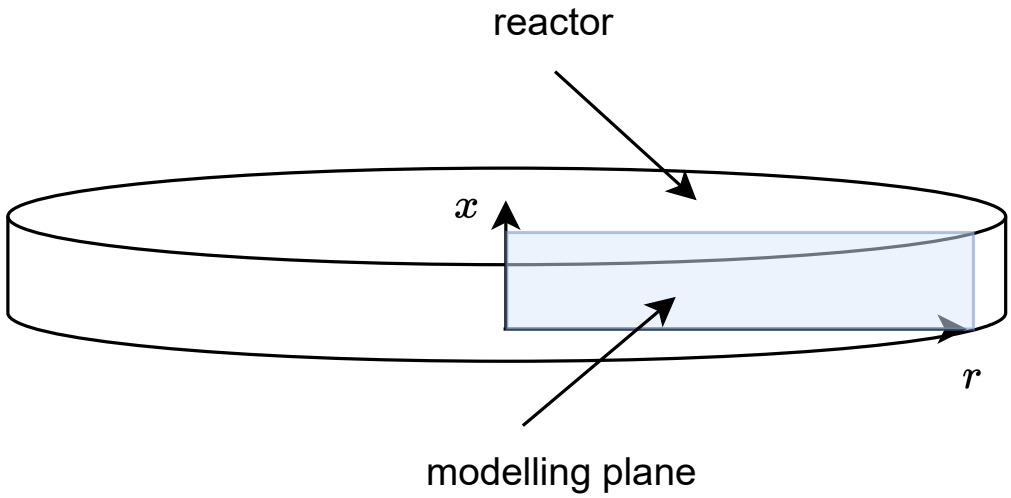

Figure 2.2.: Schematic of the used coordinate system

2.2.1. Mass Conservation

To gain information about the velocity field the conservation equations for mass and momentum need to solved. For a 2D axisymmetric case, as used here, the equations look like this [26]:

$$\frac{\partial}{\partial x}(\rho u_x) + \frac{\partial}{\partial r}(\rho u_r) + \frac{\rho u_r}{r} = 0 \tag{2.1}$$

This is the continuity equation for an in-compressible fluid where r is the radial coordinate, u_x is the axial velocity, u_r is the radial velocity and ρ is the density. In addition to the shown continuity equation the radial and axial momentum equations (Equation 2.2 and Equation 2.3) need to be solved.

$$\frac{1}{r}\frac{\partial}{\partial x}(r\rho u_x^2) + \frac{1}{r}\frac{\partial}{\partial r}(r\rho u_r u_x) = -\frac{\partial p}{\partial x} + \frac{1}{r}\frac{\partial}{\partial x}\left[r\mu\left(2\frac{\partial u_x}{\partial x} - \frac{2}{3}(\nabla \cdot \mathbf{u})\right)\right] + \frac{1}{r}\frac{\partial}{\partial r}\left[r\mu\left(\frac{\partial u_x}{\partial r} - \frac{\partial u_r}{\partial x}\right)\right] \tag{2.2}$$

$$\frac{1}{x}\frac{\partial}{\partial r}(r\rho u_x u_r) + \frac{1}{r}\frac{\partial}{\partial x}(r\rho u_r^2) = -\frac{\partial p}{\partial r} + \frac{1}{r}\frac{\partial}{\partial x}\left[r\mu\left(\frac{\partial u_r}{\partial x} - \frac{\partial u_x}{\partial r}\right)\right] + \frac{1}{r}\frac{\partial}{\partial r}\left[r\mu\left(2\frac{\partial u_r}{\partial r} - \frac{2}{3}(\nabla\cdot\mathbf{u})\right)\right] - 2\mu\frac{u_r}{r^2} + \frac{2}{3}\frac{\mu}{r}(\nabla\cdot\mathbf{u}) \tag{2.3}$$

The viscosity μ plays a role within the momentum equations, in addition to the known variables from Equation 2.1. Within all previous stated equations the product of ∇ and the velocity vector $\mathbf{u}$ can be written as:

$$\nabla\cdot\mathbf{u} \equiv \frac{\partial u_x}{\partial x} + \frac{\partial u_r}{\partial r} + \frac{u_r}{r} \tag{2.4}$$

2.2.2. Energy Equation

The energy equation mostly influences the temperature and internal energy of the mixture. The equation the software solves can be written as [26]:

$$\frac{\partial}{\partial t}(\alpha_q\rho_q h_q) + \nabla\cdot(\alpha_q\rho_q\vec{u}_q h_q) = \alpha_q\frac{\partial p_q}{\partial t} + \overline{\overline{\tau}}_q : \nabla\vec{u}_q \tag{2.5}$$

In this equation α describes the non-dimensional Helmholtz-Energy, h is the enthalpy, u is the velocity, $\overline{\overline{\tau}}$ is the stress vector and p is the pressure. Enthalpy is created by the reaction. The subscripts q stand for all different species needed to be taken into account. This equation is solved under an isothermal condition so the temperature does not change during the simulation.

2.2.3. Reaction Equation

Since the reaction $A + B \rightarrow C$ takes place where the two reactants A and B meet, the amount of product formed needs to be calculated for the whole domain. The method applied here is to calculate the reaction rate, which is dependent of the temperature and species parameters. This rate is then used to calculate the formed product. Within this work the reaction takes place only in one direction, so no backwards reaction rates are needed. The reaction rate can be calculated using this equation [26]:

$$\hat{R}_{i,r} = \Gamma\left(\nu''_{i,r} - \nu'_{i,r}\right)\left(k_{f,r}\prod_{j=1}^{N}\left[C_{j,r}\right]^{(\eta'_{j,r}+\eta''_{j,r})}\right) \tag{2.6}$$

$\hat{R}_{i,r}$ is the reaction rate, $\nu''_{i,r}$ and $\nu'_{i,r}$ are the stoichiometric numbers of the product and

reactants, $k_{f,r}$ is the rate constant for the forward reaction, $C_{j,r}$ is the molar concentration of the species j and $\eta'_{j,r} + \eta''_{j,r}$ are the rate exponents for the species j and define the reaction order. The index r loops through all reactions, in case there is more than one present. The index j is used to distinguish between different species taking part in the reaction.
To model an instantaneous product building process, the reaction constant needs to have a theoretical value of ∞. Since a discrete value needs to set for the model a large value is set to make the reaction as fast as possible. More general information about the reaction are given in Section 2.5.2 and Table 3.4 explains the reaction setup in `ANSYS FLUENT`.

2.2.4. Species Transfer Advection-Diffusion-Reaction Equations

In addition to the mentioned equations the coupled PDEs for all species must be solved. These equations, as shown in [24], can be written as:

$$\frac{\partial c_A}{\partial t} + \left(\frac{\partial u_x}{\partial x} + \frac{\partial u_r}{\partial r} + \frac{u_r}{r}\right) c_A = D\left(\frac{\partial^2 c_A}{\partial r^2} + \frac{\partial^2 c_A}{\partial x^2}\right) - k c_A c_B \tag{2.7}$$

$$\frac{\partial c_B}{\partial t} + \left(\frac{\partial u_x}{\partial x} + \frac{\partial u_r}{\partial r} + \frac{u_r}{r}\right) c_B = D\left(\frac{\partial^2 c_B}{\partial r^2} + \frac{\partial^2 c_B}{\partial x^2}\right) - k c_A c_B \tag{2.8}$$

$$\frac{\partial c_C}{\partial t} + \left(\frac{\partial u_x}{\partial x} + \frac{\partial u_r}{\partial r} + \frac{u_r}{r}\right) c_C = D\left(\frac{\partial^2 c_C}{\partial r^2} + \frac{\partial^2 c_C}{\partial x^2}\right) + k c_A c_B \tag{2.9}$$

Since the diffusion coefficients D for all species do have the same values there is no index needed. c_A, c_B and c_C are the concentration of the species A, B and C and k is the reaction constant.

2.3. Finite Volume Method

With no analytical solution available for the governing equation PDE system, numerical approaches need to be applied. `ANSYS FLUENT` which is a VOF solver is used to build the model. The method used to calculate the properties for each cell is called Finite Volume Method. The Finite Volume Method is a discretization method. It converts the set of partial differential equations into a system of linear algebraic equations [28]. This is done in two steps. At first the partial differential equations are integrated and

so transformed into balance equations [28]. The discretization step is explained in the next section.

2.3.1. Semi-Discretization

For demonstration the conservation equation for a generic variable Φ is given by [28]:

$$\underbrace{\frac{\partial(\rho\Phi)}{\partial t}}_{\text{transient term}} + \underbrace{\nabla\cdot(\rho\mathbf{u}\Phi)}_{\text{convective term}} = \underbrace{\nabla\cdot(\Gamma_\Phi\nabla\Phi)}_{\text{diffusion term}} + \underbrace{S_\Phi}_{\text{source term}} \tag{2.10}$$

Within this equation ρ represents the density and $\mathbf{u}$ is the velocity vector. ∇ contains the spacial derivatives and Γ_Φ is the diffusion coefficient of the property Φ. For an easier explanation of the maths behind the method the steady state form of Equation 2.10 is used.

$$\nabla\cdot(\rho\mathbf{u}\Phi) = \nabla\cdot(\Gamma_\Phi\nabla\Phi) + S_\Phi \tag{2.11}$$

This equation is integrated over the control volume shown in Figure 2.3, which leads to Equation 2.12.

$$\int_{V_C}\nabla\cdot(\rho\mathbf{u}\Phi)dV = \int_{V_C}\nabla\cdot(\Gamma_\Phi\nabla\Phi)dV + \int_{V_C}S_\Phi dV \tag{2.12}$$

The volume integrals, within the convective and diffusive term, can be replaced by surface integrals using the divergence theorem. That leads to the semi-discretized Equation 2.13.

$$\oint_{\partial V_C}(\rho\mathbf{u}\Phi)d\mathbf{S} = \oint_{\partial V_C}(\Gamma_\Phi\nabla\Phi)d\mathbf{S} + \int_{V_C}S_\Phi dV \tag{2.13}$$

The variable $\mathbf{S}$ is the surface vector, the operator $(\cdot)$ is the dot product and $\oint_{\partial V_C}$ is the surface integral operator.

2.3.2. Surface Integration

As seen in Equation 2.13 surface integrals are needed, to calculate the value of the property Φ for the control volume. Theses surface integrals can be split into a summation over each cell surface. This step can be done for the convective term shown in

Equation 2.14 as well as for the diffusion term shown in Equation 2.15 [28].

$$\oint_{\partial V_C} (\rho \mathbf{u} \Phi) d\mathbf{S} = \sum_{f_i}^{n_{\text{faces}}} \left(\int_f (\rho \mathbf{u} \Phi) d\mathbf{S} \right) \tag{2.14}$$

$$\oint_{\partial V_C} (\Gamma_\Phi \nabla \Phi) d\mathbf{S} = \sum_{f_i}^{n_{\text{faces}}} \left(\int_f (\Gamma_\Phi \nabla \Phi) \right) \tag{2.15}$$

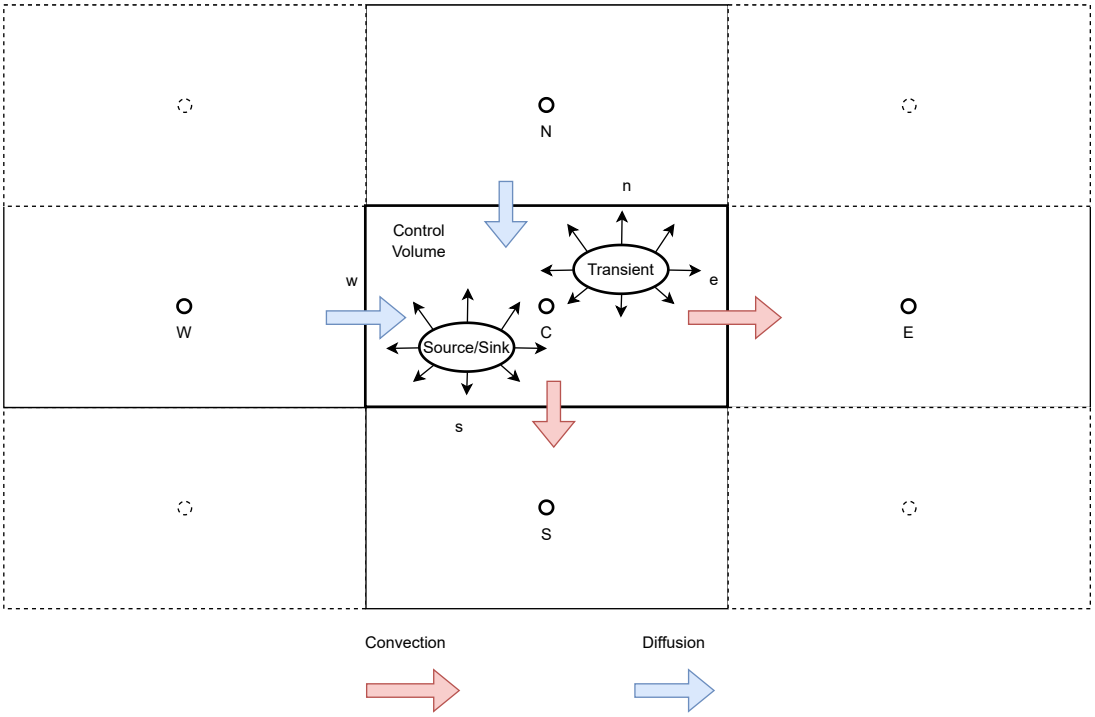

Figure 2.3.: Control Volume example

From this point on it can be seen that the values of Φ at each cells surface are needed. The solution algorithm used, calculates and stores the results only at the cell's center. To obtain values at the cells surfaces, the neighbouring cell's values are used as well. The method used here is called Quadratic upwind differencing scheme and is explained in greater detail within the following section.

2.3.3. Quadratic upwind differencing scheme

The **q**uadratic **u**pstream **i**nterpolation for **c**onvective **k**inetics [27] or QUICK as an abbreviation is used here, because it provides a reliable way of calculating a cell's properties by considering the neighbouring cells values. In addition to that it takes into account

where the flow is coming from. As shown in Figure 2.3, each cell in a 2D case has 4 neighbouring cells that are labelled N for north, S for south, E for east and W for West. The QUICK method uses the 2 neighbouring cells upward the flow direction. A schematic is shown in Figure 2.4. The cell westward to the W cell is called WW and using the same naming scheme the cell eastward to E is named EE. With a flow from

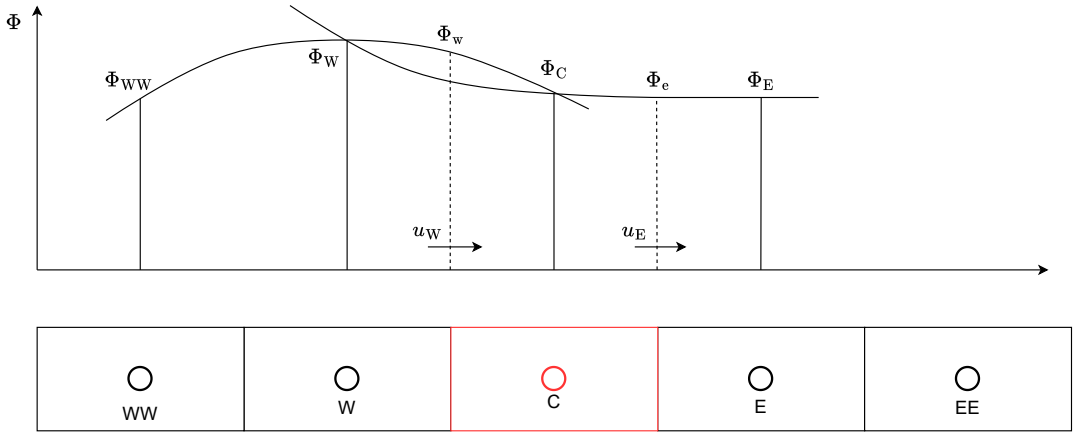

Figure 2.4.: QUICK method cell scheme

west to east through the cell with the center C, the cells surface values Φ_w for the west facing surface and Φ_e for the east facing surface are calculated as follows [27]:

$$\Phi_w = \frac{6}{8}\Phi_W + \frac{3}{8}\Phi_C - \frac{1}{8}\Phi_{WW} \tag{2.16}$$

$$\Phi_e = \frac{6}{8}\Phi_C + \frac{3}{8}\Phi_E - \frac{1}{8}\Phi_W \tag{2.17}$$

It can be seen that the method highly values the cell's direct upstream neighbour's value given the weight value of $\frac{6}{8}$, since it has the most influence on the surface value it faces. If the flow is reverse in direction the method stays the same but the cells the values are used do change.

$$\Phi_w = \frac{6}{8}\Phi_C + \frac{3}{8}\Phi_W - \frac{1}{8}\Phi_E \tag{2.18}$$

$$\Phi_e = \frac{6}{8}\Phi_E + \frac{3}{8}\Phi_C - \frac{1}{8}\Phi_{EE} \tag{2.19}$$

2.4. Solution Method

The solution method used in this case is called PISO algorithm, which stands for **P**ressure **I**mplicit with **S**plitting **O**peration algorithm. A general overview of the method's procedure can be seen in Figure 2.5 [27].
At first all fields have to be initialized with some values given by the user. With these initial values the method starts its calculation. The first step within the calculation is to get the results of the momentum equations for each cell within the mesh. The results gained are, a 2D case given, the velocity fields v^* and u^*. After this step is finished, the gained velocity fields are used to calculate the pressure correction p'. This is done by setting the pressure offset to a value that satisfies the continuity equation for the cell. With this offset p' a new pressure field p^{**} can be calculated that is then used to correct the velocity fields u^* and v^*. This correction is done in a way, similar to the already described method in subsection 2.3.3 using the values of the neighbouring cells. After the new velocity fields u^{**} and v^{**} have been gained, the PISO algorithm performs a second pressure correction. This yields the pressure field p^{***}. Now a second velocity field correction takes place, in the same manner as the first one. After that is done, all other transport equations are solved using the latest fields for the velocities u^{***}, v^{***} and the pressure p^{***}. Finally a convergence check is performed and if successful the algorithm stops. The convergence is a criterion, that does a comparison of the fields that are given as inputs and the ones yielded as outputs. If their difference is bellow a certain set threshold, the solution has converged. The threshold as to be given by the user for each variable of interest, or the default ones are used. If the resulting fields have not converged, the latest output is used as new input and the solving and corrections steps take place again. This iterative approach is done as long as the convergence criterion is not fulfilled or the maximum amount of iterations is reached.

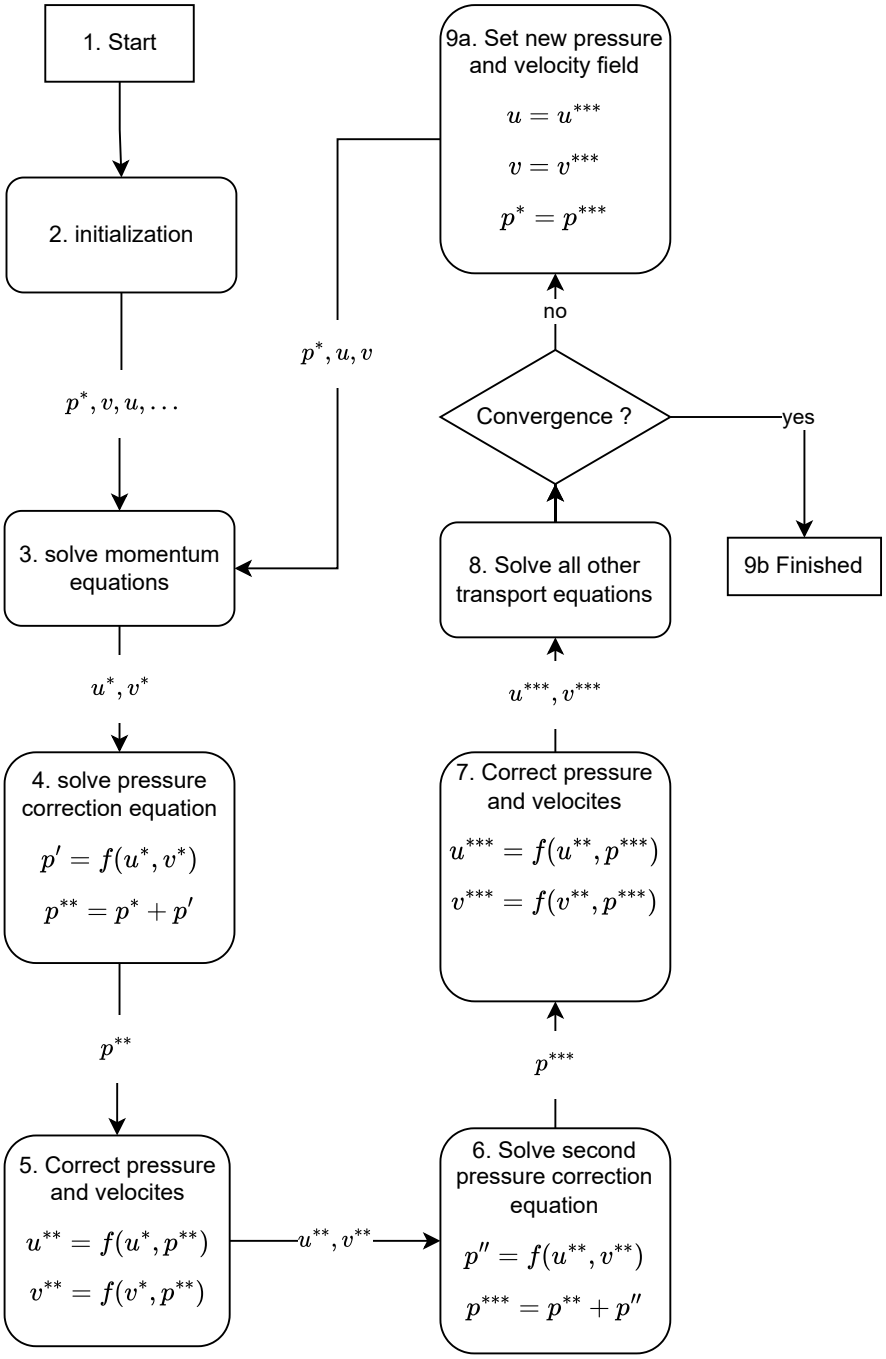

Figure 2.5.: Schematic of the steps performed within one iteration of the PISO algorithm

2.5. Flow Observations

Within a developing reaction-diffusion-advection front some specific phenomena can be observed. The main ones are looked at in this section.

2.5.1. Taylor-Dispersion

One of the phenomena taking place within a reaction-diffusion-advection front is called Taylor-Dispersion. This was first discovered by G.I. Taylor [29] in 1956. The discovered phenomenon describes the spreading of a front over time, as it can be seen within Figure 2.6. This simple example shows that the front, as marked in red within the

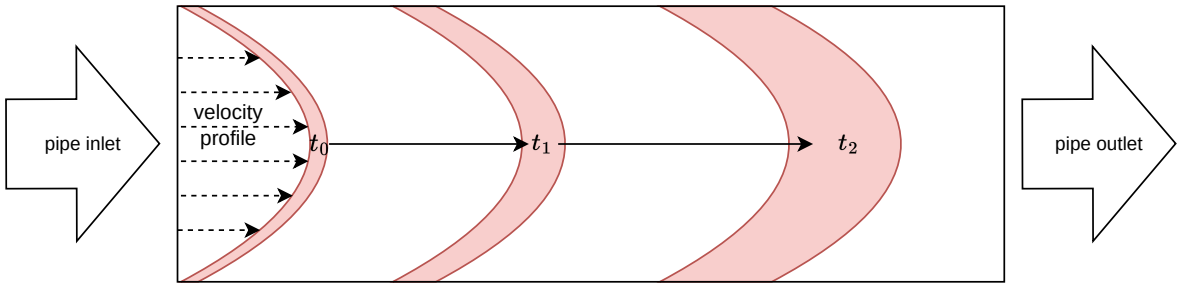

Figure 2.6.: Taylor dispersion within a pipe reactor

image, grows in width over time and distance. This growth process takes place due to diffusion within the front itself. Within the case of a radial reactor, that is investigated here, only gap averaged concentration values are available from the experiments. Within these experiments the effect of Taylor-Dispersion is visible within the gap averaged data. A schematic [3] of this effect showing within example concentration data is displayed in Figure 2.7.

As shown in Figure 2.7 the fronts concentration distribution changes along the flow direction x within the time t. The peak lowers and the distribution widens as time passes. How quickly this effect takes place and which parameters do influence it is discussed within Chapter 4. From the velocity field displayed in Figure 2.6 it can be seen that the front travels at different speeds dependent on the position at the tubes diameter. This results in a shear flow that can be described by an effective diffusion coefficient as shown in Equation 2.20 [23].

$$D_{\text{eff}} = D\left[1 + \frac{L^2 \cdot U^2}{\sigma \cdot D^2}\right] \tag{2.20}$$

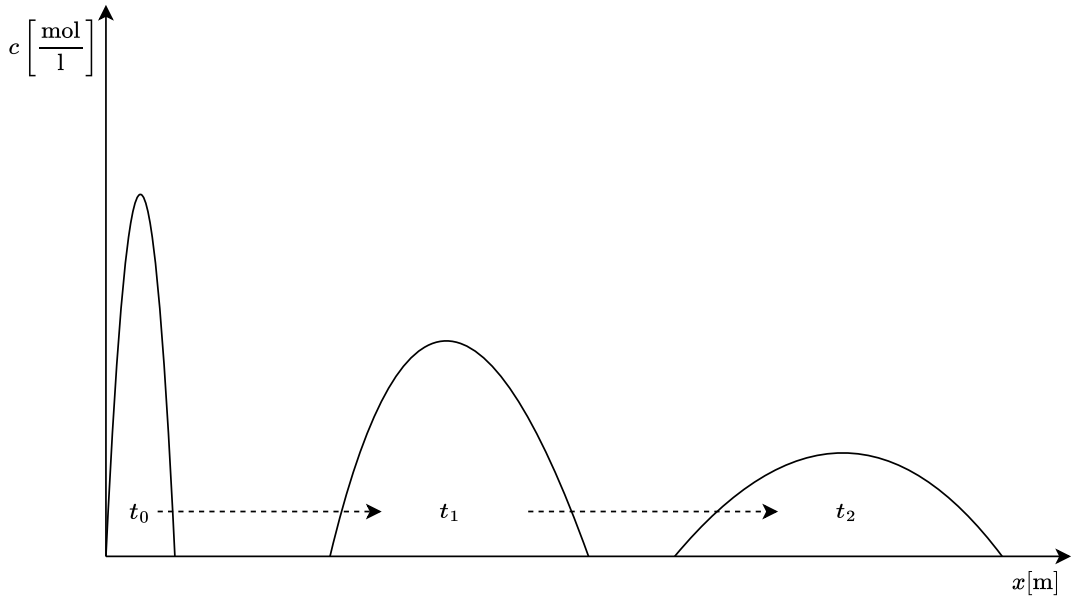

Figure 2.7.: Taylor dispersion within a radial reactor [3]

In this equation L is the characteristic length , U is the gap averaged velocity and σ is a geometric factor, that has a value of 210 for a radial case [23]. Within this work the fronts width, as well as the height averaged concentration distribution are the results looked at checking for Taylor dispersion.

2.5.2. Reaction Details

Within this section a closer look is taken at the reaction that is implemented in the model. The reaction can be described by Equation 2.21.

$$A + B \xrightarrow{r} C \tag{2.21}$$

The reaction rate r can be calculated using Equation 2.22. From this equation it can be seen that the reaction is of second order and is dependent of the species A and B.

$$r = k \cdot c_A \cdot c_B \tag{2.22}$$

The reaction velocity equation uses the rate constant k which can be computed using the context of Equation 2.23.

$$k = k_\infty \cdot e^{-\frac{E_A}{R \cdot T}} \tag{2.23}$$

Since the reaction needs to be nearly instantaneous as mentioned in Section 2.2.3 the pre-exponential factor k_∞ is set to a high value of 10^{15} $\left[\frac{\mathrm{l}^2}{\mathrm{mol \cdot s}}\right]$. The reaction takes place under isothermal conditions so the rate has a constant value. The variable E_A is the reaction's activation energy with a value of 10^4 $\left[\frac{\mathrm{J}}{\mathrm{mol}}\right]$, R is the gas constant with a value of 8.3145 $\left[\frac{\mathrm{J}}{\mathrm{mol \cdot K}}\right]$ and T is the temperature in Kelvin. The activation energy only needs to fulfill the requirement, that the reaction takes place under the given temperature conditions. This is achieved, by lowering it's value to the point the reaction shows the desired behaviour.

2.5.3. Dimensionless Variables

To be able to compare simulations and experiments, two dimensionless variables are used. These are the Schmidt number Sc and the Peclet number Pe. The Peclet number is calculated using Equation 2.24 and the Schmidt number is computed using Equation 2.25.

$$Pe = \frac{\text{advective transport rate}}{\text{diffusive transport rate}} = \frac{l \cdot u}{D} \tag{2.24}$$

The Peclet number is influenced by the characteristic length l, the inlet velocity u and the diffusion coefficient D. The characteristic length within this model is equal to the gap height. The diffusion coefficient is set to be the same one as calculated from the experiments for model validation, but is also varied during the parametric study. The inlet velocity u is calculated using the volumetric flow rate Q and the inlet's surface area at a distance of 5mm from reactors centreline.

$$Sc = \frac{\nu}{D} \tag{2.25}$$

The Schmidt number is only influenced by thermophysical constants. The diffusion constant D and the viscosity ν affect this variable. Both are adapted when changing Sc during the parametric study.

In addition to the Schmidt number and the Peclet number, the Courant number plays a role in the development process. This number is mainly of internal use within the numerical solution process. This number can be calculated using Equation 2.26. It is influenced by the velocity u, the time step Δt and the spacial discretization Δx.

$$c = \frac{u \cdot \Delta t}{\Delta x} \tag{2.26}$$

3. Simulation Model

Within this part the creation process of the simulation model will be explained in greater detail. At first the geometry modelling, meshing and solver setup will be explained. Later on, the mesh dependency study and the model validation are explained.

3.1. Model Setup

In this section the steps needed to create the model within `ANSYS FLUENT` are explained.

3.1.1. Geometry Creation

The first step of the model creation in `ANSYS FLUENT` is the modelling of the system's geometry. This geometry can either be created using the tools `ANSYS FLUENT` provides or be imported from an already existing CAD model. Within this work the geometry is created using `ANSYS DesignModeler`. In Figure 3.1 a sketch of the designed model is shown and the used dimensions are listed in Table 3.1. h represents the height of the

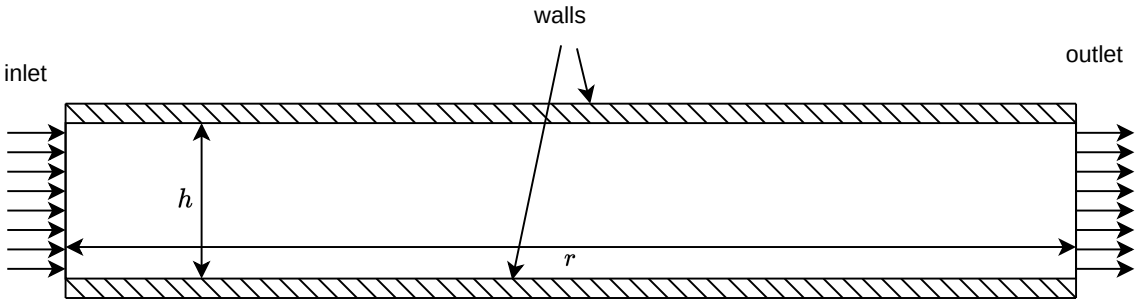

Figure 3.1.: Sketch of the model geometry including outer dimensions

Hele-Shaw cell and r is the radius of the cell.

3.1.2. Meshing

In this section the mesh creation process is explained in greater detail. An example of the generated mesh can be seen in Figure 3.2. The figure shows the reactor's inlet section. The goal in meshing this geometry, is to create a rectangular grid consisting of squares

Table 3.1.: Used values for geometry dimensions

variable	value	unit
r	30.0	mm
h	0.2...0.6	mm

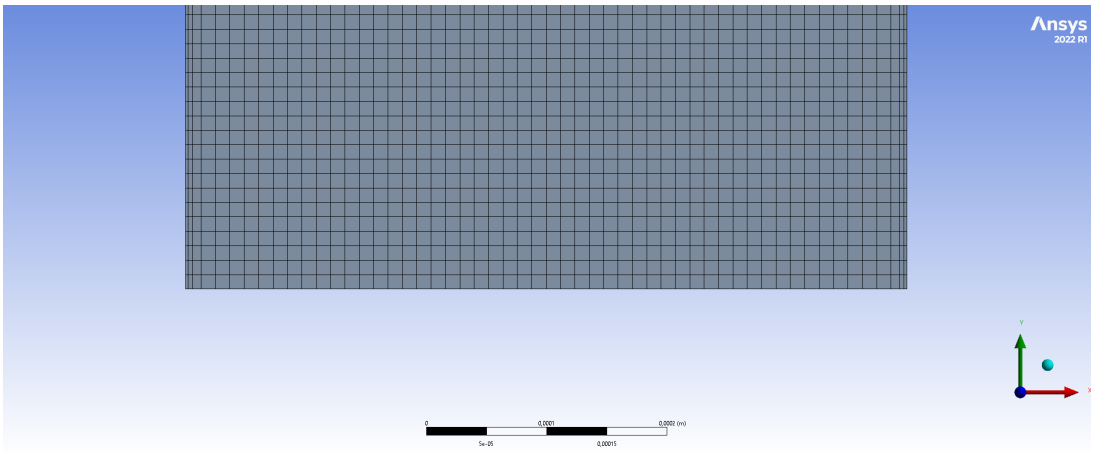

Figure 3.2.: Ansys Meshing example

or rectangles. Near the walls, that begin on the left and right side of the inlet, the mesh resolution is increased using two inflation layers. That is done to resolve the boundary layer of the flow near the walls. These finer resolutions near the wall are needed, because near the wall the flows velocity does show large gradients [27]. Having a mesh consisting mostly out of squares and rectangles is advantageous because the algorithm only stores the values at the cell's centre as mentioned in Section 2.3.3 and having a mesh that can be seen as a 2 dimensional array helps with post-processing. The detailed results and their analysis are discussed in Section 3.3.2.

3.1.3. Solver Settings

To setup the model, a few general configuration steps need to done at first. The Settings that need to be applied are listed in Table 3.2.
The type of solver chosen is a Pressure-Based, that also is the default value. The velocity formulation is set to `Absolute`, because the input velocity is set to an absolute value. The `Time` setting is set to `Transient`, because the flow modelled is not stationary and

Table 3.2.: General model settings

Section	Setting	value
Solver	Type	Pressure-Based
Solver	Velocity Formulation	Absolute
Solver	Time	Transient
Solver	2D Space	Axisymmetric

the interest is in results during the whole models simulation run. The `2D Space` settings has a value of `Axisymmetric` due to the axisymmetric nature of the geometry. The Viscous model is set to `Laminar` because laminar flow conditions are used. Due to a reaction being part of the model, the energy variable needs to be set to `On`.
After the correct models are turned on and parametrized, the species taking part within the model are defined. Within this case 4 fluids are needed. The example configuration of one of the fluids taking part within the reaction is shown in Table 3.3. The table shows the configuration of one of the reactants. All other values, namely enthalpies and

Table 3.3.: Example fluid mixture settings for one of the reactants

variable	value	unit
ρ	1000	$\frac{\mathrm{kg}}{\mathrm{m}^3}$
ν	1.0e-6...1.2e-6	$\frac{\mathrm{m}^2}{s}$
D	1.00e-10...8.22e-10	$\frac{\mathrm{m}^2}{s}$

other thermodynamic properties are the same for all the fluids and equal to the values of water. Since 3 fluids take part in the reaction and 4 fluids are needed to setup the model, the yet missing fluid is water. It is needed to be able to set a molar concentration at the inlet. With the mixture settings done, the reaction parameters are set next. The parameters set for the reaction are stated in Table 3.4. To achieve a nearly instant reaction when molecules of the two species A and B meet, the rate constant which is also known as Pre-Exponential Factor (see Equation 2.6) is set to $1 \cdot 10^{15} \left[\frac{\mathrm{l}^2}{\mathrm{s \cdot mol}}\right]$. The Activation Energy is set to a value of $1 \cdot 10^4 \left[\frac{\mathrm{J}}{\mathrm{mol}}\right]$. With that value, the given temperature of 300[K] is high enough to let the reaction happen. After the reaction is setup correctly, the boundary conditions are being set. Boundary conditions need to be set for the inlet,

Table 3.4.: Reaction settings

variable	value	unit
Reaction Type	Volumetric	-
Stoich. Coefficient fluid_a	1	-
Stoich. Coefficient fluid_b	1	-
Stoich. Coefficient fluid_c	1	-
Rate Exponent fluid_a	1	-
Rate Exponent fluid_b	1	-
Rate Exponent fluid_c	0	-
Pre-Exponential Factor	1e15	$\frac{\mathrm{l}^2}{\mathrm{s \cdot mol}}$
Activation Energy	1e4	$\frac{\mathrm{J}}{\mathrm{mol}}$

outlet and the walls. All information needed to configure the boundary conditions are visible in Table 3.5. As part of the boundary conditions the flow domain has to be initialized with values to start the simulation from. To achieve the same conditions as within the experimental setup the reactor is filled with species B with a concentration of 0.03 $\left[\frac{\mathrm{mol}}{\mathrm{l}}\right]$. Mole fractions x_i are required as inputs for the inlet, so they have to be calculated from the given concentration using Equation 3.1.

$$\begin{aligned} x_{fluid\_a} &= \frac{\dot{n}_{fluid\_a}}{\dot{n}_{fluid\_a} + \dot{n}_{water}} \\ &= \frac{c_{fluid\_a} \cdot Q}{c_{fluid\_a} \cdot Q + c_{water} \cdot Q} \\ &= \frac{c_{fluid\_a}}{c_{fluid\_a} + c_{water}} \end{aligned} \tag{3.1}$$

The initialization of the domain requires mass fractions φ_i so they need to be calculated as well using Equation 3.2. In addition to the mass fraction, the internal domain is initialized with a pressure of 20[Pa] and a temperature of 300[K]. To get a homogenous velocity profile at the inlet normal to the boundary, the specification method is set to `Magnitude, Normal to Boundary`.

$$\begin{aligned} \varphi_{fluid\_b} &= \frac{n_{fluid\_b} \cdot M_{fluid\_b}}{n_{fluid\_b} \cdot M_{fluid\_b} + n_{water} \cdot M_{water}} \\ &= \frac{c_{fluid\_b} \cdot M_{fluid\_b}}{c_{fluid\_b} \cdot M_{fluid\_b} + c_{water} \cdot M_{water}} \end{aligned} \tag{3.2}$$

Table 3.5.: Models boundary conditions

place	variable	value	unit
inlet	Type	velocity-inlet	-
inlet	Velocity Specification Method	Magnitude, Normal to Boundary	-
inlet	Velocity Magnitude	8.33e-5...4.21e-3	$\frac{\mathrm{m}}{\mathrm{s}}$
inlet	Temperature	300	K
inlet	x_{fluid_a}	5.4e-4	-
outlet	Type	pressure-outlet	-
outlet	Gauge Pressure	20	Pa
outlet	Prevent Reverse Flow	yes	-
wall	Type	wall	-
wall	Shear Condition	No Slip	-

In Table 3.6 the properties of the species taking part in the reaction are shown. The molar masses for species A and B are the same and the product C has a value that is twice as high compared to the values of the species A or B. The molar masses are set that way to ensure the reaction $A + B \rightarrow C$ takes place with one mole of A and B do result in one mole of product C. The densities are set to $1000\left[\frac{\mathrm{kg}}{\mathrm{m}^3}\right]$ for all species.
The temperature is set to 300[K] at the inlet. The outlet is configured to be a pressure outlet without reverse flow, to get physically valid results. At the walls the usual conditions applied to walls are set with `No slip`.
The next step performed is to setup the solution methods as shown in Table 3.7. As the solving scheme the PISO algorithm is used, that is explained in section 2.4. For spatial discretization second order methods, as explained in subsection 2.3.3, are used.
As a last step in the model creation procedure the time discretization parameters need to be set. An adaptive method is chosen, which is based on the CFL-Number c. The CFL-Number is another name for the Courant number. It is best practice to keep this number below or equal to 1 for stability reasons. This can be otherwise thought of as a limiting factor in a way, that to rapid changes from one cell to the next one between time steps are inhibited.
In this model the Courant number is set to 1 and the initial time step size is set to the same value as the minimum time step. The time step size is updated after every calculation. The factor for time step changes are limited to 0.5 on the lower end and 2 at the upper end. The time step algorithm decides on how much the current time step needs to be adapted, based on the Courant number. In most cases the time step used

Table 3.6.: Mixture species properties

variable	description	value	unit
M_{water}	Molar Mass water	18	$\frac{\mathrm{g}}{\mathrm{mol}}$
M_{fluid_a}	Molar Mass $fluid\_a$	100	$\frac{\mathrm{g}}{\mathrm{mol}}$
M_{fluid_b}	Molar Mass $fluid\_b$	100	$\frac{\mathrm{g}}{\mathrm{mol}}$
M_{fluid_c}	Molar Mass $fluid\_c$	200	$\frac{\mathrm{g}}{\mathrm{mol}}$
ρ_{water}	Density water	1000	$\frac{\mathrm{kg}}{\mathrm{m}^3}$
ρ_{fluid_a}	Density $fluid\_a$	1000	$\frac{\mathrm{kg}}{\mathrm{m}^3}$
ρ_{fluid_b}	Density $fluid\_b$	1000	$\frac{\mathrm{kg}}{\mathrm{m}^3}$
ρ_{fluid_c}	Density $fluid\_c$	1000	$\frac{\mathrm{kg}}{\mathrm{m}^3}$
c_{fluid_a}	Concentration $fluid\_a$	0.03	$\frac{\mathrm{mol}}{\mathrm{l}}$
c_{fluid_b}	Concentration $fluid\_b$	0.03	$\frac{\mathrm{mol}}{\mathrm{l}}$
x_{fluid_a}	molar fraction $fluid\_a$	5.4e-4	-
x_{fluid_b}	molar fraction $fluid\_b$	5.4e-4	-
φ_{fluid_a}	mass fraction $fluid\_a$	3e-3	-
φ_{fluid_b}	mass fraction $fluid\_b$	3e-3	-

by the solver has a value close to the minimum time step size of values around 0.001 seconds. The minimum time step is set dependant on the inlet velocity. In addition to the model's time settings, the interval the results are exported at need to be set. More information on the model's implementation can be found in Section A.2.

Table 3.7.: Solution methods

tab	setting	method
Pressure-Velocity Coupling	Scheme	PISO
Spatial Discretization	Pressure	Second Order
Spatial Discretization	Momentum	QUICK
Spatial Discretization	$fluid\_a$	Second Order Upwind
Spatial Discretization	$fluid\_b$	Second Order Upwind
Spatial Discretization	$fluid\_c$	Second Order Upwind
Spatial Discretization	Energy	Second Order Upwind

Table 3.8.: Time discretization parameters

variable	value	unit
Type	Adaptive	-
Method	CFL-Based	-
Duration Specification Method	Total Time	-
Total Time	60...360	s
Courant Number	1	-
Fixed Timsteps	1	-
Initial Time Step Size	1e-4...2.5e-3	s
Max Iteration/Time Step	30	-
Time Step Size Update Interval	1	-
Minimum Time Step Size	1e-4...2.5e-3	s
Maximum Time Step Size	0.5	s
Minimum Step Change Factor	0.5	-
Maximum Step Change Factor	2	-

3.2. Model Evolution

Here the steps taken to receive the final model for each case are explained.

3.2.1. Mesh Dependency

To achieve trustworthy results from a CFD-model the solution obtained should not be dependent of the grid element size. Therefore a mesh dependency study is performed. The results are shown here for the case with a gap height of 0.4mm. In Figure 3.3 the results of the average wall shear stress calculations for different grid element sizes are shown. In the displayed case the average wall shear stress does increase for very coarse meshes. The mesh chosen, as marked with read, is gained by a linear interpolation. The final mesh used for this case has approximately 600.000 elements, which results in a good compromise between mesh density and computational effort needed for solving. The mesh dependency results for the other cases can be found in Section A.1.

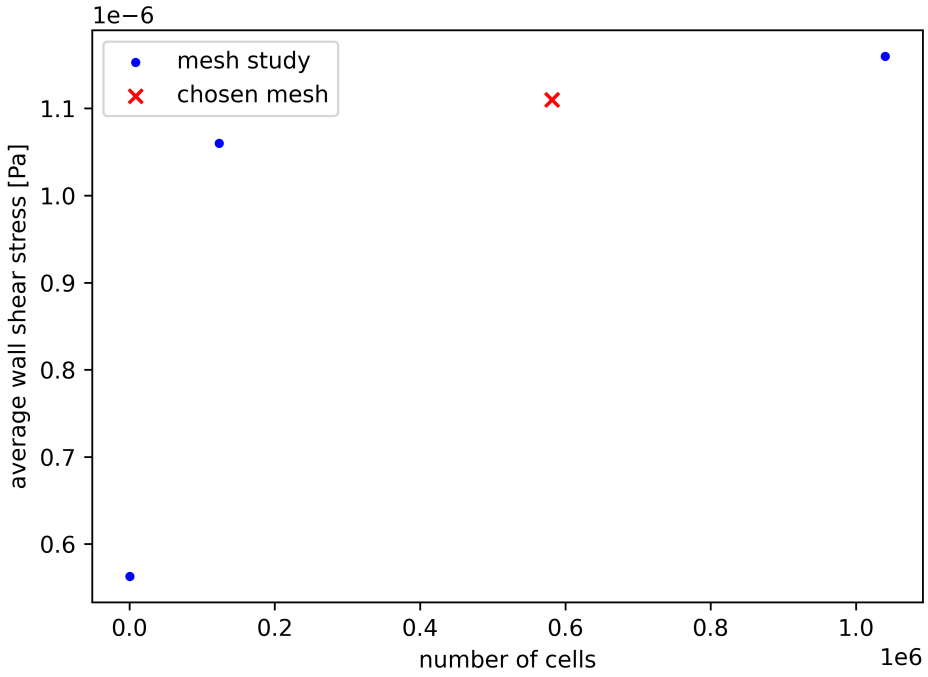

Figure 3.3.: Mesh dependency study for geometry with 0.4mm gap height

The results of a false mesh in combination with false settings are exemplary shown in Figure 3.4. With this method a fine enough mesh for each case is chosen, so that the

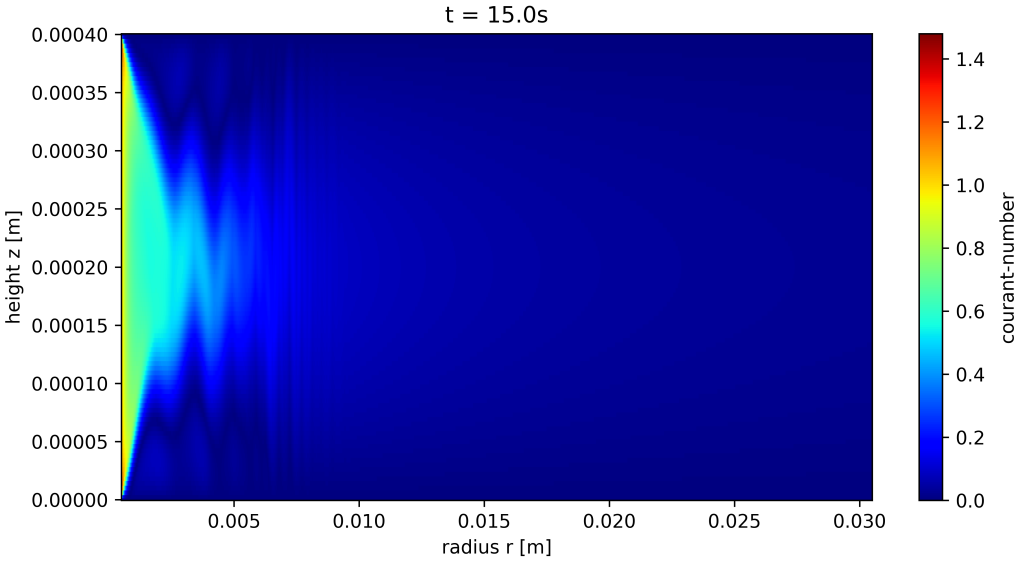

(a) Wrong Courant number field for an example case

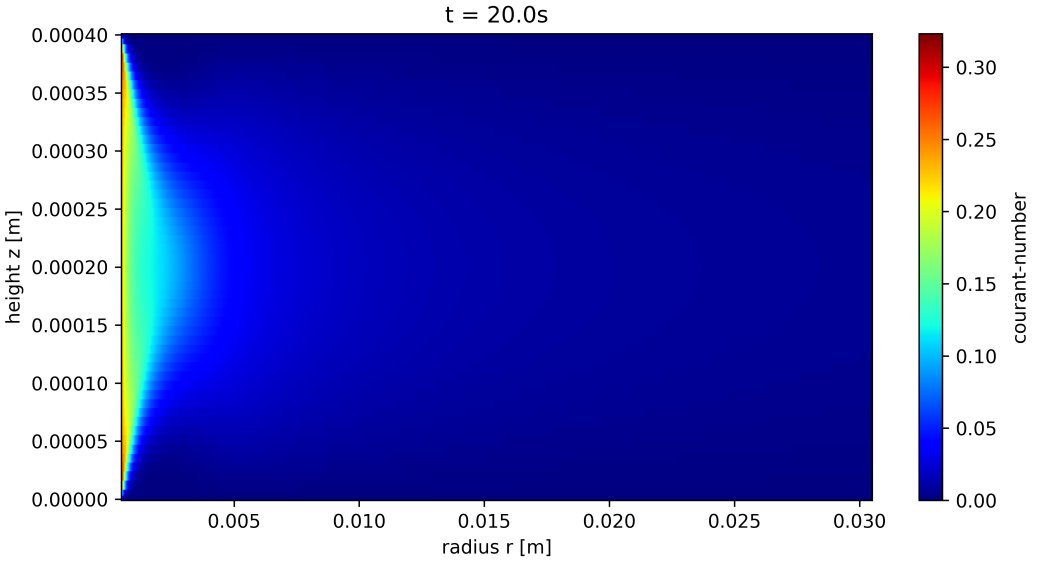

(b) Right Courant number field for another example case

Figure 3.4.: Right and wrong example of Courant number field

results can be trusted.

3.2.2. Cases Setup

For the Peclet-Number 3 different values are chosen and for the Schmidt number 2 values are implemented. These values are in case of Pe 500, 931 and 2050. The Peclet number values are set to close values experimental data is available for. The Schmidt number Sc has either a value of 2430 or 12000. The lower value is chosen to match existing experimental results and the higher one set to see a significant change compared to the lower one. The Schmidt number mostly influences the diffusion coefficient, as the viscosity ν does not change a lot between the two chosen values. Having fixed the Schmidt number and the diffusion coefficient, the Peclet-Number mostly influences the input velocity. An overview of the performed cases and their input variable values can be seen in Table 3.9. Besides the reactor height h, the Peclet-Number Pe and other needed input variables, the simulation time and export time in seconds need to be set. The simulation time is the physical time, that represents for how long the model should be simulated. The export time sets the time interval in seconds at which results are exported during the transient simulation. These results, that contain all the values for all variables of interest for each cell, are the basis for further analysis. Section 3.3.2 explains how the results are further processed in more detail.

Table 3.9.: Simulation cases parameter values

h [m]	Pe	Sc	ν [m^2/s]	D [m^2/s]	u [m/s]	x_A	φ_B	simulation time [s]	export time [s]
2.00E-04	500	2430	1.00E-06	4.11E-10	1.03E-03	5.40E-04	3.00E-03	60	0.5
2.00E-04	500	12000	1.20E-06	1.00E-10	2.50E-04	5.40E-04	3.00E-03	60	0.1
2.00E-04	500	120000	1.20E-06	1.00E-11	2.50E-05	5.40E-04	3.00E-03	60	0.1
2.00E-04	931	2430	1.00E-06	4.11E-10	1.91E-03	5.40E-04	3.00E-03	60	0.5
2.00E-04	931	12000	1.20E-06	1.00E-10	4.66E-04	5.40E-04	3.00E-03	60	0.1
2.00E-04	931	120000	1.20E-06	1.00E-11	4.66E-05	5.40E-04	3.00E-03	60	0.1
2.00E-04	2050	2430	1.00E-06	4.11E-10	4.21E-03	5.40E-04	3.00E-03	60	0.5
2.00E-04	2050	12000	1.20E-06	1.00E-10	1.02E-03	5.40E-04	3.00E-03	60	0.1
2.00E-04	2050	120000	1.20E-06	1.00E-11	1.02E-04	5.40E-04	3.00E-03	60	0.1
4.00E-04	500	2430	1.00E-06	4.11E-10	5.14E-04	5.40E-04	3.00E-03	60	0.5
4.00E-04	500	12000	1.20E-06	1.00E-10	1.25E-04	5.40E-04	3.00E-03	60	0.1
4.00E-04	500	120000	1.20E-06	1.00E-11	1.25E-05	5.40E-04	3.00E-03	60	0.1
4.00E-04	931	12000	1.20E-06	1.00E-10	2.33E-04	5.40E-04	3.00E-03	60	0.1
4.00E-04	931	2430	1.00E-06	4.11E-10	9.57E-04	5.40E-04	3.00E-03	60	0.5
4.00E-04	931	120000	1.20E-06	1.00E-11	2.33E-05	5.40E-04	3.00E-03	60	0.1
4.00E-04	2050	12000	1.20E-06	1.00E-10	5.12E-04	5.40E-04	3.00E-03	60	0.5
4.00E-04	2050	2430	1.00E-06	4.11E-10	2.10E-03	5.40E-04	3.00E-03	60	0.5
4.00E-04	2050	120000	1.20E-06	1.00E-11	5.12E-05	5.40E-04	3.00E-03	60	0.1
6.00E-04	500	2430	1.00E-06	4.11E-10	3.43E-04	5.40E-04	3.00E-03	60	0.5
6.00E-04	500	12000	1.20E-06	1.00E-10	8.33E-05	5.40E-04	3.00E-03	60	0.5
6.00E-04	500	120000	1.20E-06	1.00E-11	8.33E-06	5.40E-04	3.00E-03	60	0.5
6.00E-04	931	12000	1.20E-06	1.00E-10	1.55E-04	5.40E-04	3.00E-03	60	0.5
6.00E-04	931	2430	1.00E-06	4.11E-10	6.38E-04	5.40E-04	3.00E-03	60	0.5
6.00E-04	931	120000	1.20E-06	1.00E-11	1.55E-05	5.40E-04	3.00E-03	60	0.5
6.00E-04	2050	12000	1.20E-06	1.00E-10	3.41E-04	5.40E-04	3.00E-03	60	0.5
6.00E-04	2050	2430	1.00E-06	4.11E-10	1.40E-03	5.40E-04	3.00E-03	60	0.5
6.00E-04	2050	120000	1.20E-06	1.00E-11	3.41E-05	5.40E-04	3.00E-03	60	0.5

3.3. Validation

Within this chapter the model validation is explained and described. At first the experimental setup used in the performed experiments is shown and then the experimental and model results are explained. After that a comparison is done to show that the model is performing as expected.

3.3.1. Experimental Setup and Results

The experiments used for validating the developed model were done using a sounding rocket. The mission's name was TEXUS-57. The experimental setup as shown in [2] is visible in Figure 3.5. The Hele-Shaw gap is formed by two plates sitting on top of each

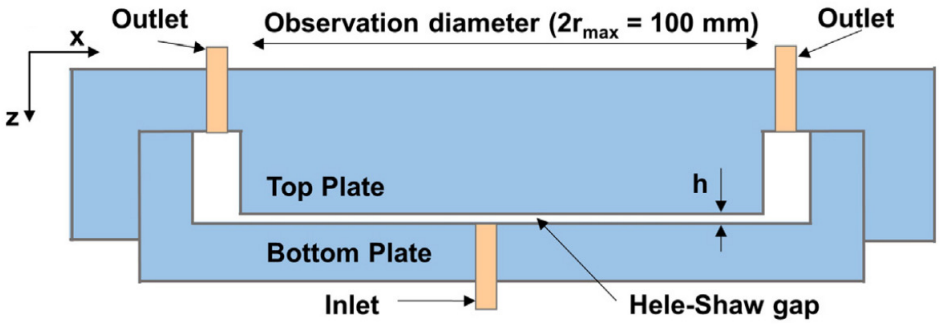

Figure 3.5.: Experimental setup used to generate existing experimental data used for validation [2]

other. The inlet is located on the bottom at the centreline of the reactor. The outlets are located at the top with an empty space, that is needed to get no influence from outlet on the flow field within the gap. The gap height h used for the experiments was 0.2mm. The experiment is observed by a camera from the top throughout the whole run. The gained images are further analysed by image processing. The images are captured as greyscale images. The gained grey values are correlated to concentration values using the known values for the initial concentrations. Based on the gained product concentration values, the reaction front's front and back positions are calculated using a threshold operation. The position of the fronts maximum is computed, by detecting the position of the maximum grey value within the image. In addition to the front's positions the total amount of product formed is calculated. This is done by integrating the concentration values over the whole domain and gap height.

3.3.2. Model Results

The model results are created at each interval defined by the user as described in Section 3.1.3. The gained tables do have a format similar to Table 3.10. The values for each cell are stored in one of the table rows. The cells are distinguishable by their x and y coordinate.

Table 3.10.: Simulation output table example

nodenumber	x-coordinate	y-coordinate	...	concentration-fluid_c	...
1	1.206592076E-06	5.0E-04	...	5.681614735E-11	...
...	...	...	...	...	...
100	1.382432295E-06	5.12E-04	...	3.607185187E-17	...
...	...	...	...	...	...

All values needed are accessible with these tables, but for further analysis the values need to be converted into a field similar to the created mesh shown in Figure 3.2 during model setup. An example of such a resulting field is shown in Figure 3.6. These fields can

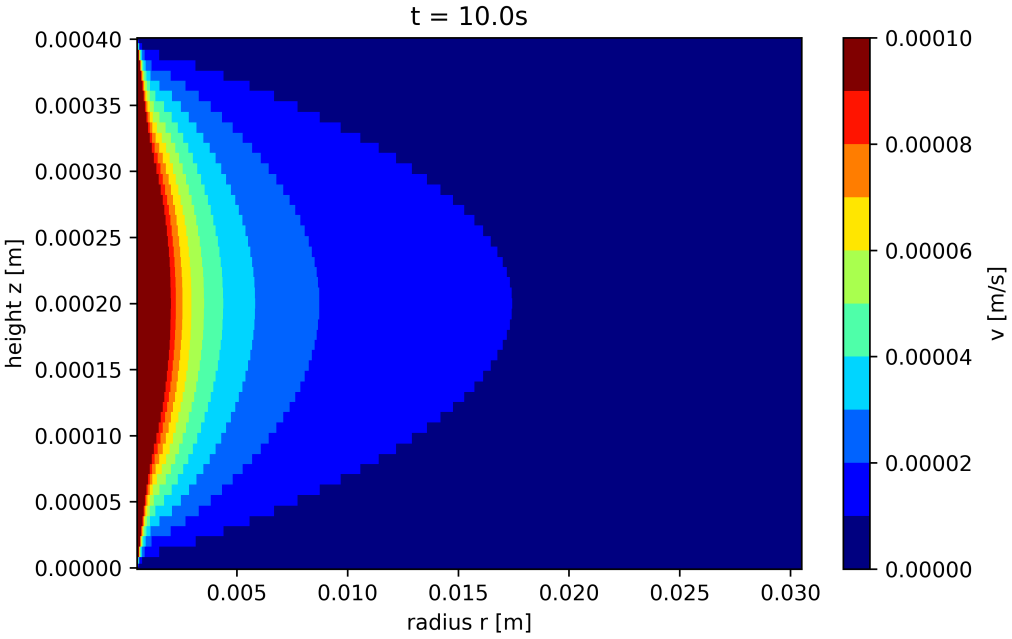

Figure 3.6.: Example field representation (velocity field) of model results

be created for all exported variables. Within the example shown the field is created for

the velocity magnitude, but the variable of most interest is the product concentration. A field example for that variable is shown in Figure 3.7 for 3 different time steps. With

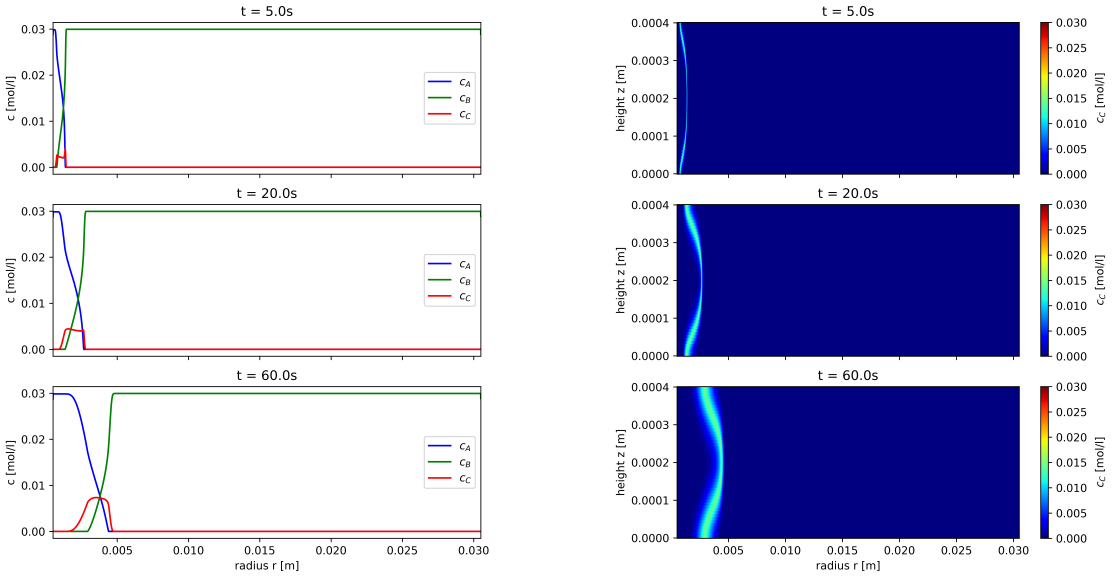

(a) gap averaged concentrations

(b) product concentration fields

Figure 3.7.: Field and averaged concentration example

these fields, the products concentration can be averaged over the whole gap height. This step is done to get a comparable post-processing step to the image processing done on the experimental data sets. The resulting plots from the previous example can also bee seen in Figure 3.7.
With the fields and the gap averaged concentration values computed the parameters of interest can be calculated. How that is done is explained within the following sections.

Front Positions

The front's maximum position is gained by storing the radial positions of the product's maximum within the concentration plots. The front's front position is calculated by using the position furthest away from the center at half the maximums value. The positions gained are shown for one time step in Figure 3.8 as an example.

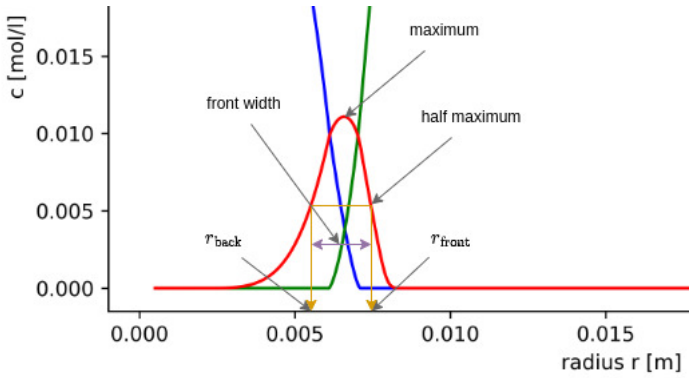

Figure 3.8.: Front position procedure schematic

Front Width

For calculating the front widths the front's front and back positions are needed. The front position is already gained and the back position is computed using the same approach. Instead of taking for furthest position away from the center the closest one to the inlet is taken to get the back position. The difference between these two radial positions is the front's width at the time. The width calculated is visualized in Figure 3.8. The approach for calculating the width is also known as **F**ull **W**idth at **H**alf **M**aximum or FWHM in short.

To gain some more insights, a second width is computed. The second width is calculated at the middle of the gap height using the same procedure. The width at half of the reactor's gap height, also described as **F**ull **W**idth at **H**alf **M**aximum at **H**alf **G**ap **H**eight, is called FWHMHGH in short. Instead of taking the gap averaged values, the values used here are the field values themselves at half the gap height. This width that is only calculated using one height position, behaves similar to a 1D case with a decaying velocity towards high radial values.

The difference between the two calculated widths is that the FWHM is influenced by the concentration values in the whole gap, compared to the FWHMHGH that is only influenced by the concentration values along the radial position at a constant height. The FWHMHGH is expected to only grow, whereas the FWHM could grow and shrink dependent on the fronts curvature.

Product Formed

Since the cell volume and the product concentration for each cell are accessible from the exported results, the total amount of product formed can be calculated by multiplying these two columns with each other. `ANSYS FLUENT` computes it's values for one radiant for a 2D axisymmetric case. To gain the amount of product within the whole reactor the values have to be multiplied by 2π. This procedure can be described by Equation 3.3. $n_{C,total}$ is the total amount of product produced, n_{cells} is the amount of cells in the mesh, V_i is the volume of one cell and $c_{i,C}$ the product's concentration within that cell i.

$$n_{C,total} = 2\pi \cdot \sum_{i=0}^{n_{cells}} [V_i \cdot c_{i,C}] \tag{3.3}$$

3.3.3. Comparison

For comparison the position of the gap averaged product's maximum values are used. From Figure 3.9 it can be seen that the model and experiment perform similar over the whole time range with a small deviation at early time steps. These differences might come from slightly different flow conditions, some premixing or other experimental uncertainties. Another reason the differences could come from, is that the experiments where carried out in 3D, whereas the model represents just a 2D case. Some non uniformities might show up during the experiment since it can't be guaranteed that the flow conditions are the same for all positions with the same radius at the same height.
All in all the model provides valid results as shown in the graph.

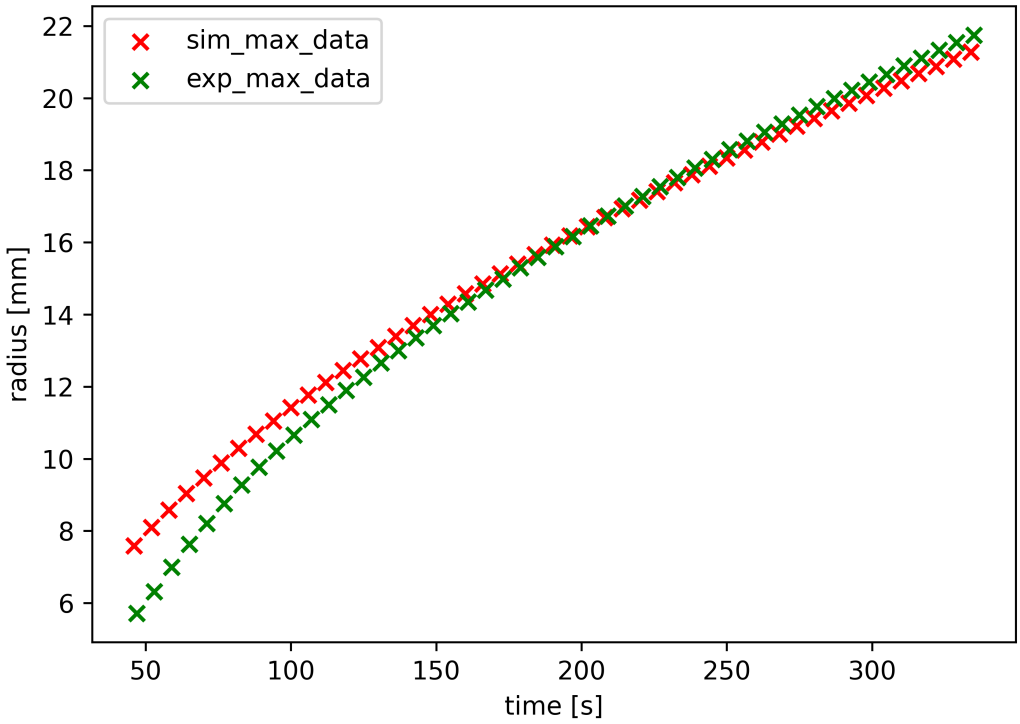

Figure 3.9.: Comparison of the experimental and model maxima positions

4. Parametric Study

The parametric study is done, to distinguish between the influence of the thermophysical properties, against the one coming from convection on the front's shape and metrics. To achieve that different inlet velocities are used to investigate the influence of convection. To get the influence of the thermophysical properties different diffusion coefficients and viscosities are set. This results in the combination of parameters studied as shown in Table 3.9.
Within the parametric study three different reactor geometries are simulated. The different conditions set for each case lead to different front shapes. Two of these front shapes for two example cases can be seen in Figure 4.1. Comparing the cases shown in

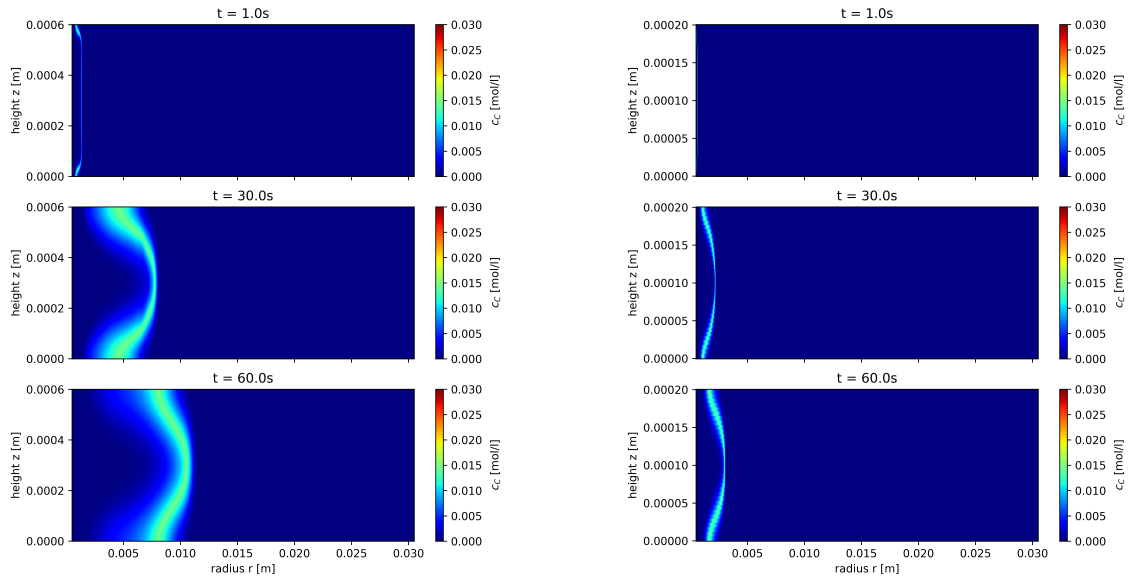

(a) Front shape for h = 0.6mm Pe = 2050 Sc = 12000

(b) Front shape for h = 0.2mm Pe = 2050 Sc = 2430

Figure 4.1.: Two example front shapes as a result of different flow conditions

Figure 4.1 it becomes clear, that the reactor gap height and thermophysical properties show a significant influence on the fronts progression and curvature. In addition to that

the front's width is also influenced. A more detailed analysis of the front's position, width and the total amount of product formed is given in the following sections.

4.1. Front Positions

The front positions behave in a similar way for all 3 reactor geometries. In Figure 4.2 and Figure 4.3 the positions for both Schmidt numbers are shown for the geometry containing a gap height of 0.2mm. The plots for the other two gap heights can be found in Section A.3. For a Schmidt number of 12000 the values for r_{front} and r_{max} do show a

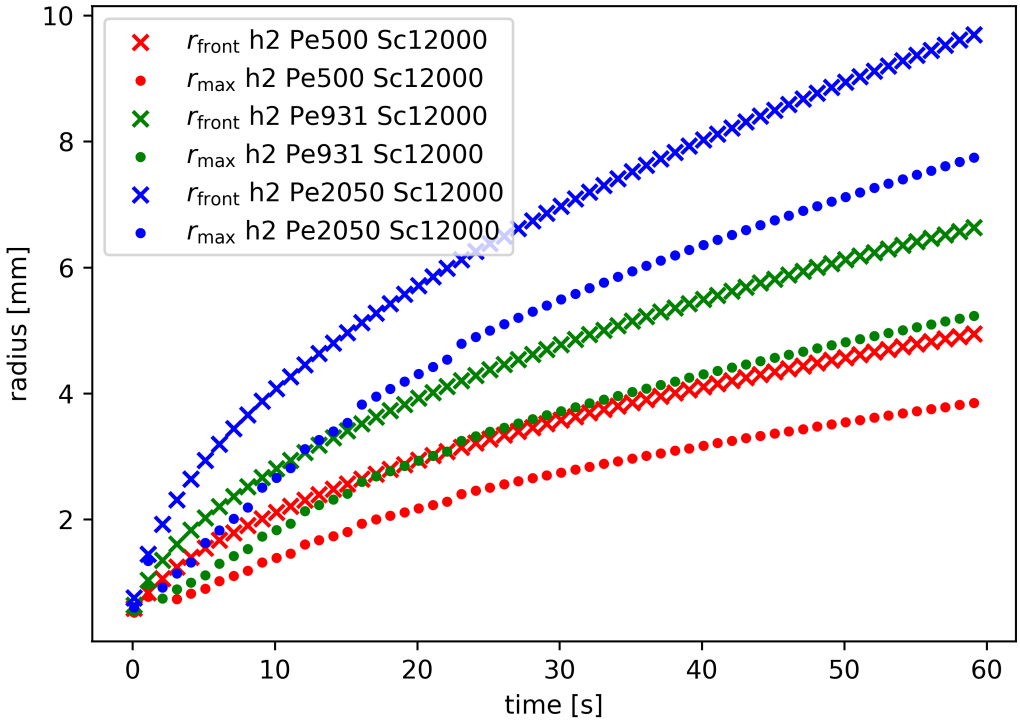

Figure 4.2.: Front positions for h = 0.2mm Sc = 12000

similar behaviour on a principle level. The r_{front} positions travel speed decays over time and seems to follow an approach close to a square root function. The values for r_{max} do show the same behaviour, but are always at lower radial values than the front values r_{front}.

The described behaviour is the same for the cases with Sc = 2430.

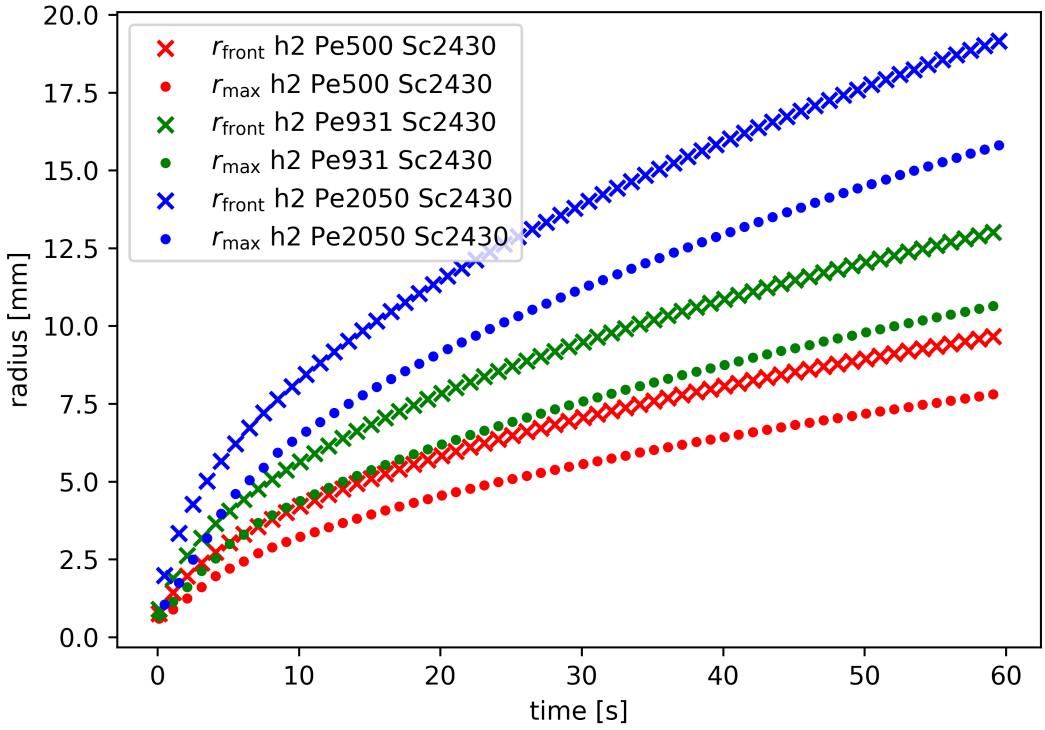

Figure 4.3.: Front positions for h = 0.2mm Sc = 2430

The r_{front} and r_{max} positions travel faster for higher Peclet numbers, which can be explained by the different input velocities. With decreasing inlet velocity, the difference between the fronts front and maximum position at later time steps decreases. The decrease is more significant for cases with higher Peclet numbers. For cases with lower Peclet numbers the distance between r_{front} and r_{max} at the end is approximately the same. This can be seen in Figure 4.3 when looking at the plots for Pe = 500 and comparing it with the ones for Pe = 931. For these cases, due to their lower absolute inlet velocity, the distance between the front's front and maximum is smaller and doesn't change that much if the velocity is risen or lowered.

When comparing the plots for Schmidt number 2430 with the one for a Schmidt number of 12000 it can be observed that all fronts travel nearly double the distance within the same time of 60 seconds. This can be explained mainly by the lower diffusion coefficient for the higher Schmidt number case. The diffusion coefficient for the lower Schmidt number case is $4.11 \cdot 10^{-10} \left[\frac{\text{m}^2}{\text{s}}\right]$ and the one for the higher Schmidt number case is

$1.0 \cdot 10^{-10} \left[\frac{\mathrm{m}^2}{\mathrm{s}}\right]$. In addition to the global Peclet number introduced in Equation 2.24 a local one can be defined using Equation 4.1.

$$Pe_{\mathrm{local}} = \frac{h \cdot u(x,r)}{D} \tag{4.1}$$

In this equation the local velocity $u(x,r)$ at the coordinates x and r is used instead of the inlet velocity u used within the global Peclet-Number. Since the velocity magnitude decreases very quickly for a axisymmetric reactor (see Figure 3.6) Pe_{local} does show the same behaviour as they are directly linked to each other. As the Peclet number is defined as the advective transport rate divided by the diffusive transport rate, a low local Peclet number means that diffusion plays a more and more significant role while the front travels through the reactor.
The diffusion coefficient has not only an influence on the front's position. The front's width is affected by diffusion as well. The fronts width will be analysed within the following section.

4.2. Front Widths

The fronts width behaviour is quite different for each reactor geometry, so each one will be looked at starting with the smallest gap height of 0.2mm. The front widths for that geometry are shown in Figure 4.4 and Figure 4.5 for each investigated Schmidt number. Within the plot for the Schmidt number of 12000, it can be seen that the width using the gap averaged product concentration data (FWHM) starts growing fast within the first seconds. After that the widths growth slows down and the width reaches it's maximum value. When the maximum has been reached the width starts shrinking slowly towards a final constant value. The FWHMHGH does show a different behaviour. Its growth starts slow within the first few seconds and then starts to follow a square root like approach towards a final constant value. The widths do reach higher values for higher Peclet numbers. For the case with a Schmidt number of 2430 the width's growth in the beginning is even faster compared to the cases with the higher Schmidt number. This faster growth can be seen for both the FWHM as well as the FWHMHGH. The decrease after the front has reached it's maximum value is more visible for the lower Schmidt number cases. From these cases it can be seen that both calculated widths seem to be driven towards the same value for later times. The same behaviour is expected to happen at later times for the simulation in the cases with Sc = 12000, which no results

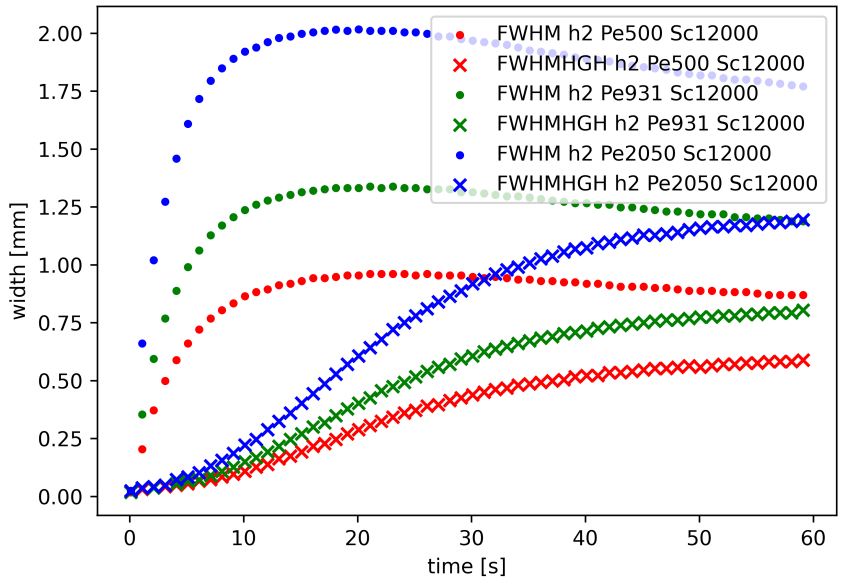

Figure 4.4.: Front widths for h = 0.2mm Sc = 12000

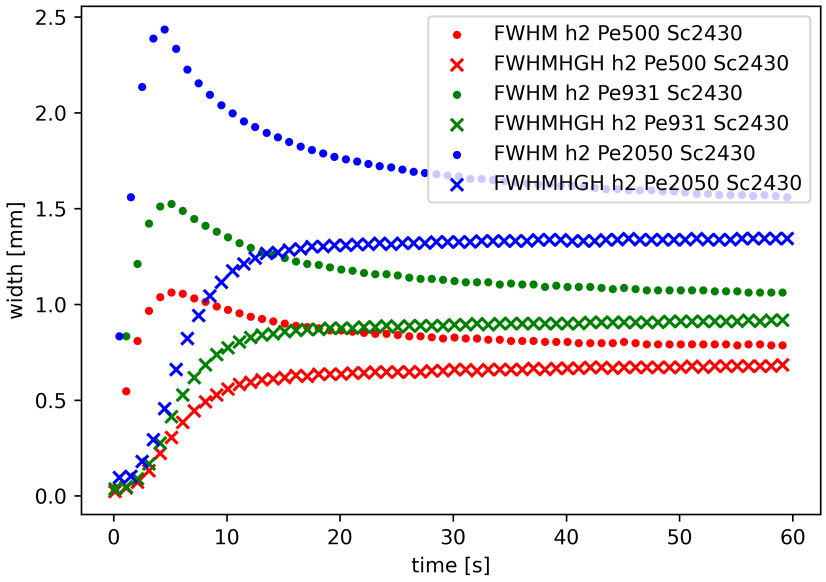

Figure 4.5.: Front widths for h = 0.2mm Sc = 2430

are calculated for.
The reason for the initial high growth is, that the front is near the inlet and new reactants are constantly available due to the high flow rate in that region. In addition to that the front's width has low values so the distance both reactants A and B need to travel to reach each other to form the product C is low. In the beginning the front's shape can be represented by a straight line, which gets distorted over time as visible in Figure 4.1a. This distortion creates new surface area for the reaction to take place, in addition to the area generated by the front's travelling in a radial reactor.
The strive towards the same value for both the FWHM and the FWHMHGH at later times can be explained by the fronts shape. In Figure 4.6 the product concentration field is shown at the time of 60 seconds, for the case with a Peclet number of 500 and a Schmidt number of 2430. When the front reaches the shown shape, the difference

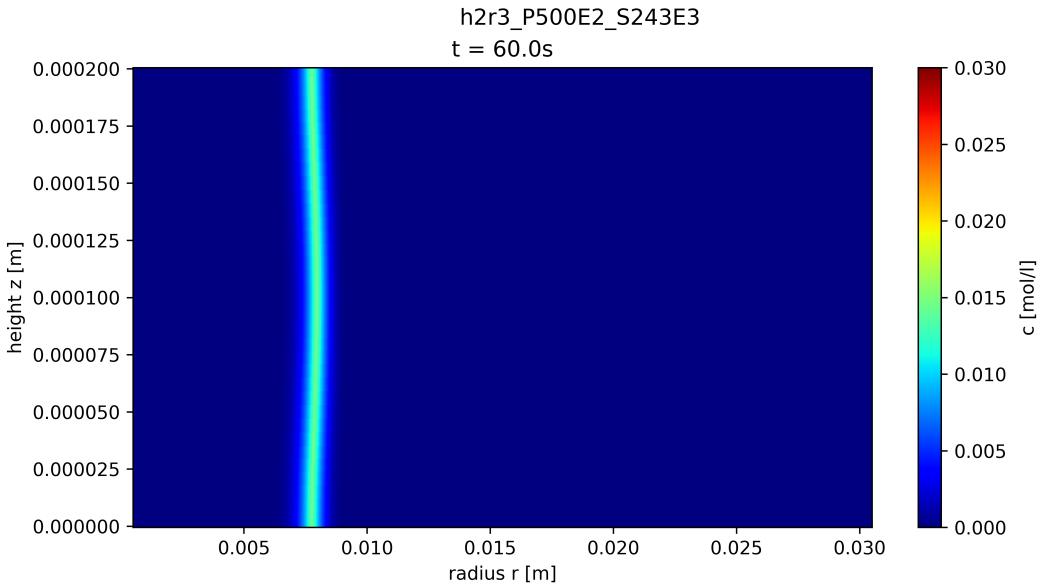

Figure 4.6.: Front shape for h=0.2mm Pe = 500 Sc = 2430 at 60 seconds

between the width using the FWHM method and the middle with decreases. As shown in [24], the reaction decays until the spreading of front by diffusion forms an equilibrium with the reactants consumed by the reaction.
Another reason for the decay could be that the maximum value changes, so the positions the widths are taken from do change as well. In Figure 4.7 the gap averaged concentration plots are shown for a time of 2 seconds which is in the phase of width growth, a time of 5 seconds which is close to the maximum and a time of 18 seconds which is near the end

of the decaying phase. From this plot it can be seen, that the curvature does change over time. It widens at first when comparing the curves for $t = 2s$ with $t = 5s$ and then narrows down. In addition to that the maximum value raises, since more product is generated over time. With the maximum value raising, the position of $0.5 \cdot c_{C,max}$ changes as well towards the more narrow section of the curve.
When comparing both Schmidt number plots with each other, it can be observed that the final width's value seems to be independent of the Schmidt number for a gap height of 0.2mm. For this gap height that is true for both the FWHM and the FWHMHGH. The results from the 0.4mm case also support this assumption for the FWHM. To get clearer evidence if the assumption is correct, more Schmidt numbers need to be investigated and the simulations should be run for longer durations. These longer durations are also needed to get a clearer picture on how the FWHMHGH behaves at later stages of the simulation run.
Another observation that can be made, is that the time the width reaches its maximum value and the maximum value itself is strongly influenced by the Schmidt number. For the lower Schmidt number of 2430 a clear peak is visible for all Peclet numbers. This forming peak seems to be expected, because the diffusion coefficient for the case with the higher Schmidt number of 12000 is lower than the one for the lower Schmidt number of 2430. A lower diffusion coefficient prevents the front from spreading so the width reaches higher values.

The results for the cases with a gap height of 0.4mm show in most parts a similar behaviour compared to the case with a gap height of 0.2mm. For the case with the higher Schmidt number of 12000 the FWHM follows a square root like approach for all Peclet numbers. For the first 3 to 5 seconds the FWHM has very low values then starts to grow suddenly. The time the growth starts to happen is higher for lower Peclet numbers. The FWHMHGH has very low values over the hole simulation time for all Peclet numbers investigated. This width's growth seems to slightly increase at later times of around 40 seconds.
The cases with the lower Schmidt number do show a comparable behaviour to the one for the height of 0.2mm, that do have the same Schmidt number. The FWHM curves show peaks as well but they are not that sharp and narrow compared against the ones in Figure 4.5. The FWHMHGH behaves similar to the one with the same conditions at 0.2mm gap height, but the phase of growth is way longer and the constant value is reached near the end ot the 60 second simulation run time.

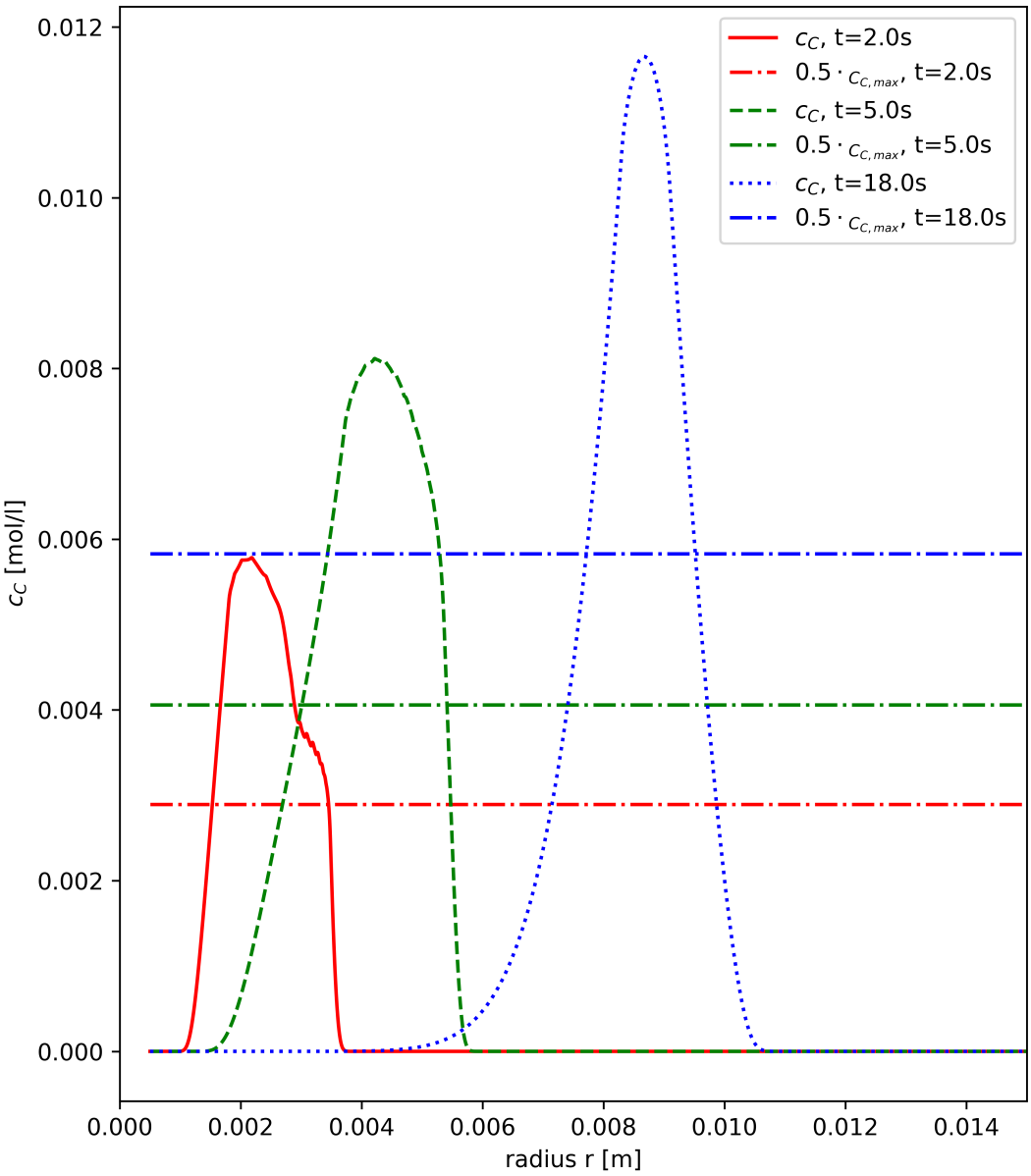

Figure 4.7.: Product concentration plots for h = 0.2mm Pe = 2050 Sc = 2430 for different times

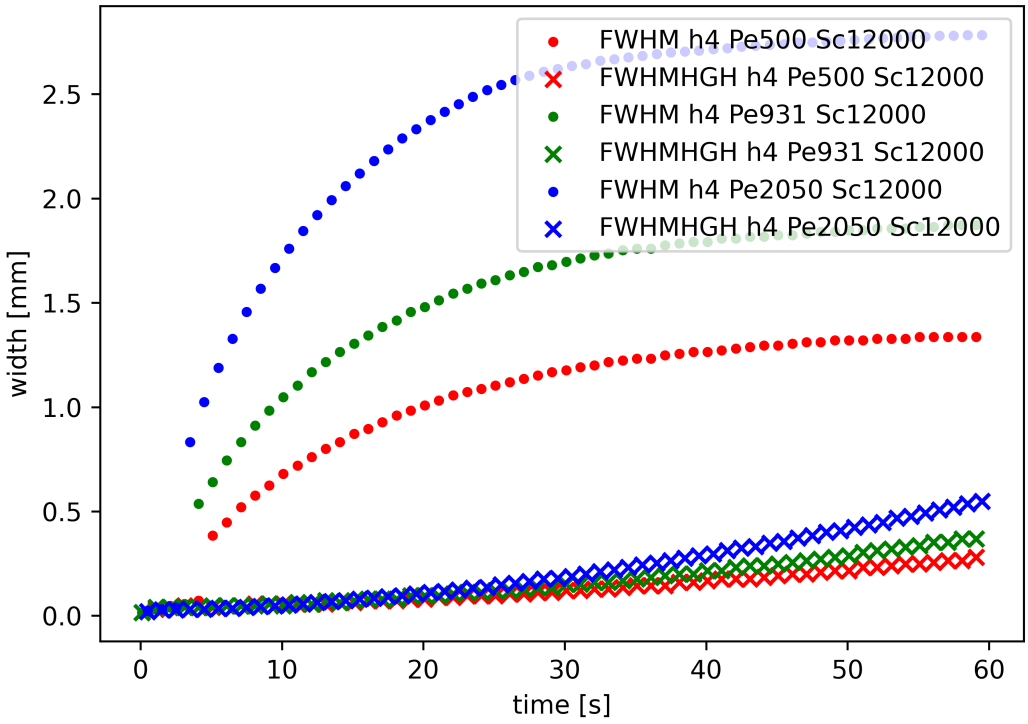

Figure 4.8.: Front widths for h = 0.4mm Sc = 12000

The square root like behaviour of the higher Schmidt number case can be explained by the fact, that the front is still in the phase of growing. This is comparable to the 0.2mm gap height cases for a time range of up to 20 seconds. For later times the FWHM is expected to decay as well as can be seen for the 0.2mm cases. The sudden growth is even more clearly visible for the gap height of 0.6mm and therefore explained there. The low growth rate of the FWHMHGH is the result of the high local Peclet number during most of the part of the simulation. The diffusive part only starts affecting this width at later times where the advective part loses it's influence on the front.
For the cases with the Schmidt number of 2430 the FWHM seems to reach it's highest value in the moment when the initial two different peaks visible within the concentration plots merge into one, which can be seen in Figure 4.10. Up to a time of around 18 seconds two peaks can be distinguished within the product concentration plots. These two peaks are visible within the concentration plots, because the local Peclet number has lower values in the areas close to the walls. As a result of that, diffusion becomes

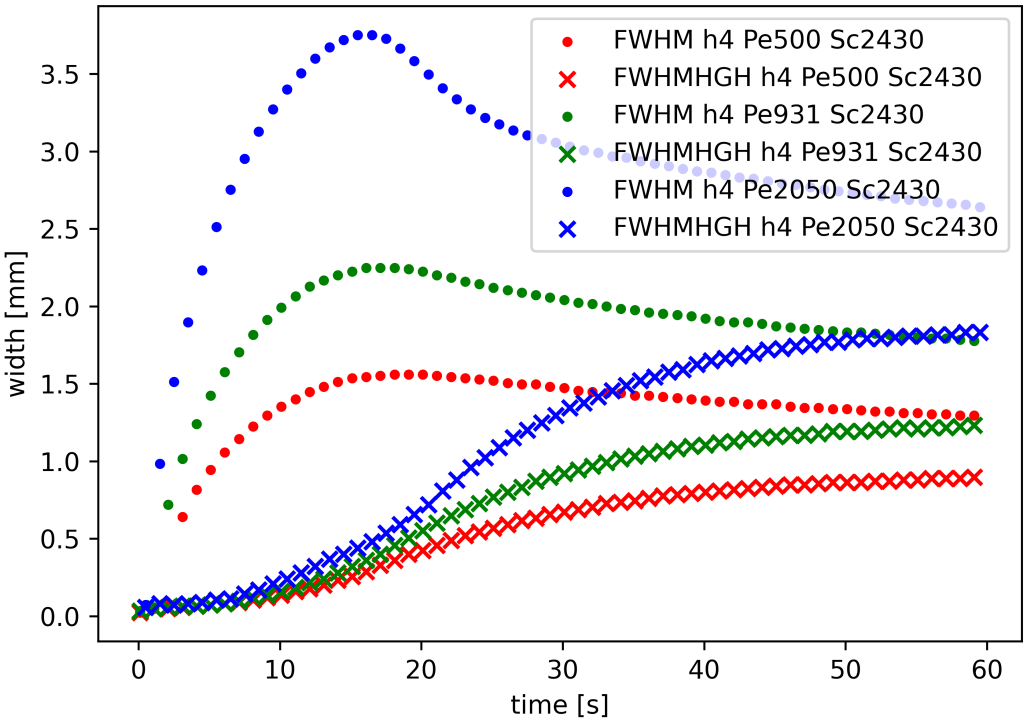

Figure 4.9.: Front widths for h = 0.4mm Sc = 2430

more dominant in these regions, even at early times. This is clearly visible when looking at the product's concentration field at a times of 2 and 10 seconds in Figure 4.11. The gap averaging operation then produces a large value in the front and back, that can be seen for the time of 2 seconds.

At the time around 18 seconds the front shape has reached it's maximum distortion. Within the gap averaged plot it can be seen that there is a sharp increase at the fronts front and a slow decline at its back. This decline lowers when comparing the plots for a time of 18 seconds with the one at 60 seconds in Figure 4.11.

The FWHMHGH behaviour can be explained using the local Peclet number. At early times the front is near the inlet, where the values are high so the influence of diffusion, which is the main mechanism driving the front's spreading is low. Diffusion along the radial direction is the main factor, because at half the gap height the flow does not experience any shear. Advection is mainly moving the front through the reactor. While leaving the advection influence zone the FWHMHGH starts growing more rapidly, since

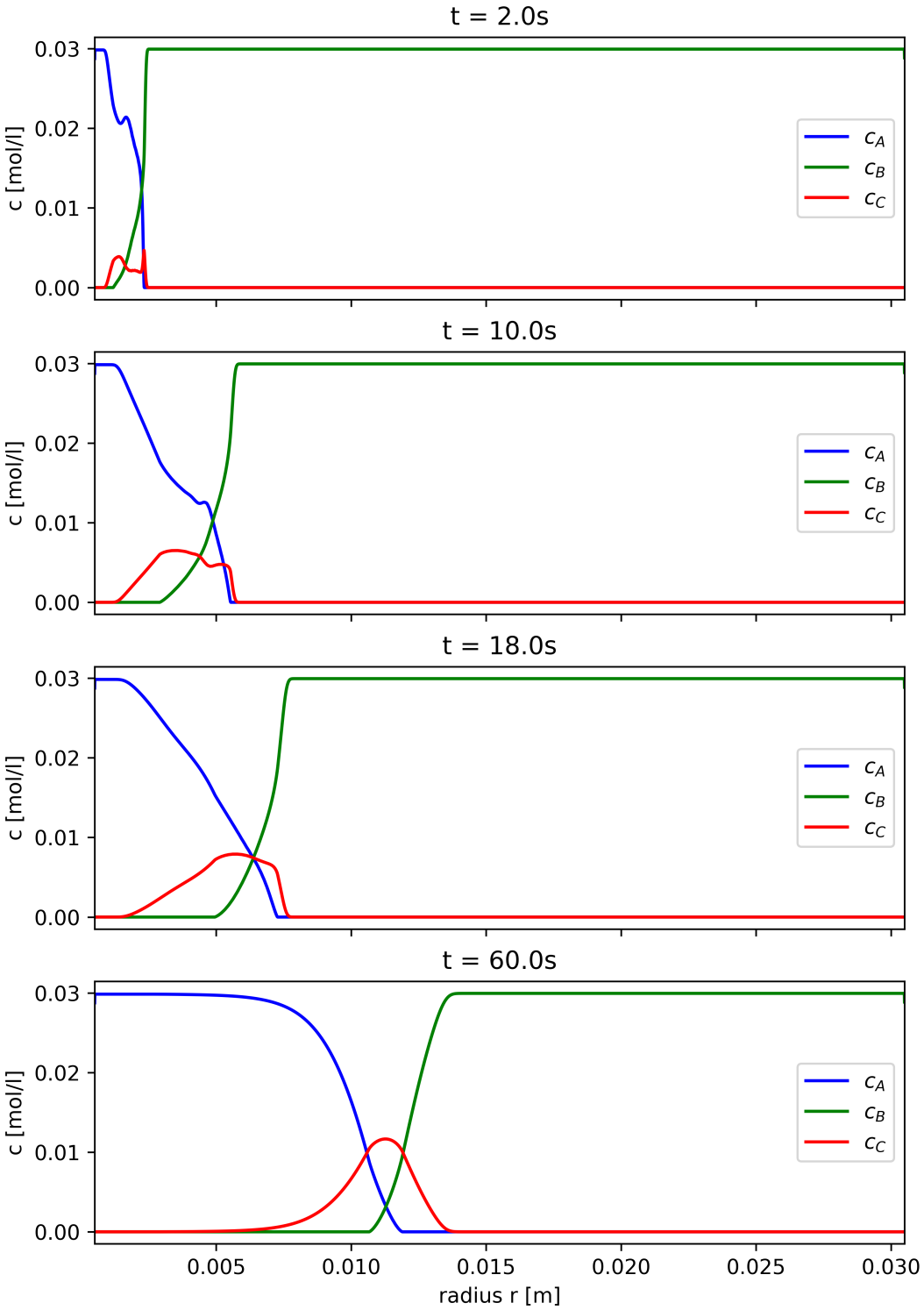

Figure 4.10.: Plots for gap averaged concentrations for h = 0.4mm Pe = 2050 Sc = 2430

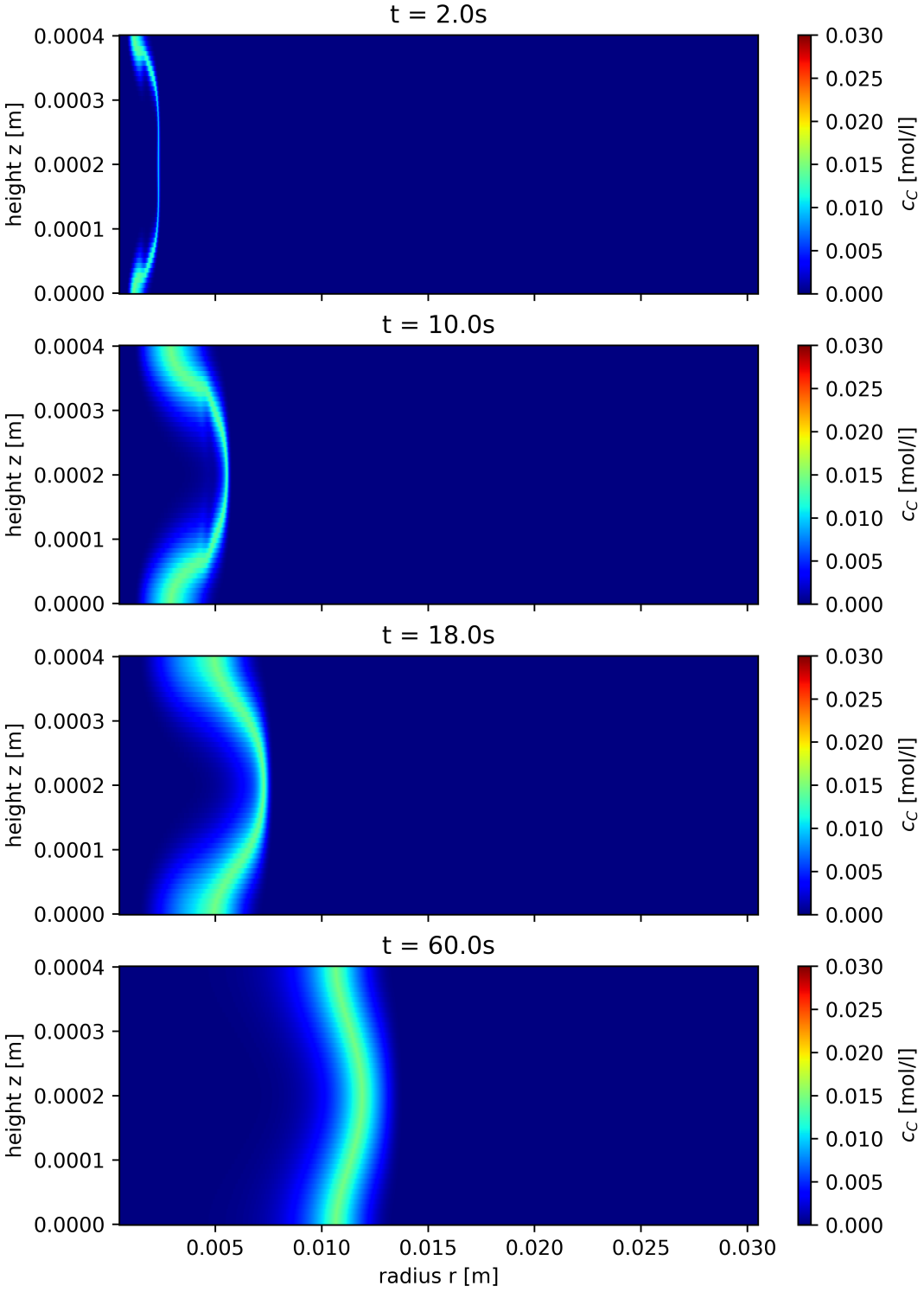

Figure 4.11.: Field for product concentration for h = 0.4mm Pe = 2050 Sc = 2430

diffusion start more and more dominating the width's growth process. The width's growths then slows down and reaches a constant value due the fact, that an equilibrium between diffusion and the reaction is reached. The differences in the FWHMHGH curves, when comparing different Schmidt numbers, can be explained by different diffusion coefficients. The higher the diffusion coefficient the sooner the growth starts and the final constant value is reached sooner as well.

For the case with a gap height of 0.6mm the width's behaviour seems to change quite significantly compared to the 0.4mm case. For the Schmidt number of 12000 the width's

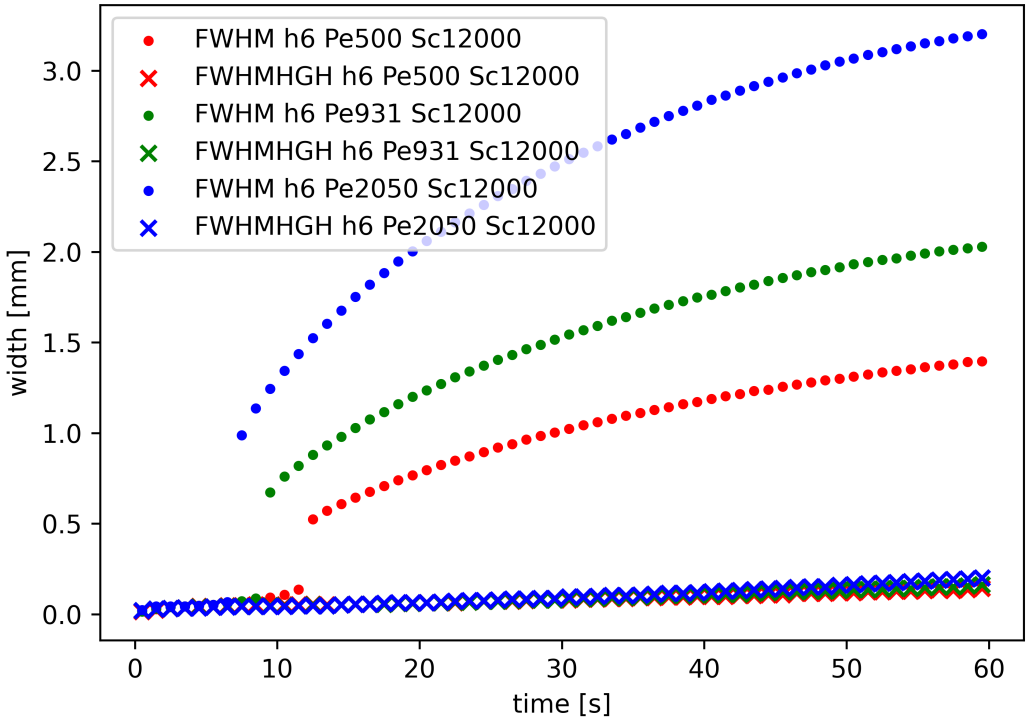

Figure 4.12.: Front widths for h = 0.6mm Sc = 12000

results are shown in Figure 4.12. The general form of the FWHM curves seems to match the ones from the previous discussed cases. A difference, compared to the 0.4mm cases, is that the width's growth seems to start delayed even more at around 8 to 12 seconds. The FWHMHGH does not grow at all for this Schmidt number. For the lower Schmidt number, shown in Figure 4.13, the peak within the FWHM plot widens even more compared to the previous cases and the maximum value is reached at later times. The FWHMHGH does not grow a lot for the first 20 seconds, but after that the widths growth rate starts increasing.

The growth delay, that can be seen for the Schmidt number of 12000 for the gap height of 0.4mm in Figure 4.8 and for the same Schmidt number for a gap height of 0.6mm in Figure 4.12, can be explained using the concentration plots. Within Figure 4.14 the concentration plots are shown for the gap height of 0.4mm and 0.6mm for a Peclet num-

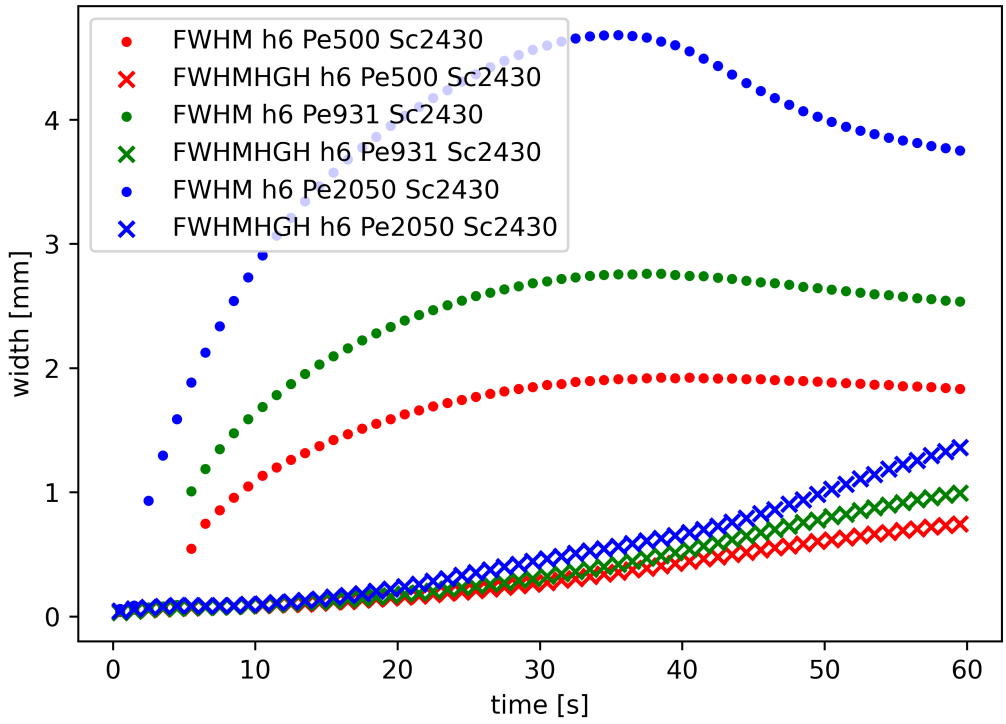

Figure 4.13.: Front widths for h = 0.6mm Sc = 2430

ber of 931 and a Schmidt number of 12000 close to the inlet. Within these two plots it can seen that the initial spike in the front start decaying over time. The moment the value of $0.5 \cdot c_{c,max}$ falls into the region above 0 and below the value at the back of the front, the front's width suddenly increases to a higher value. The FWHMHGH only reaches very low values and doesn't grow much within the 60 seconds runtime of the simulation. The reason for that behaviour is the same as discussed for the 0.4mm case. The influence of diffusion starts dominating the front's spreading at later radial values, due to a higher local Peclet number near the inlet. In the case of the higher Schmidt number the diffusion process does not seem get starting within the 60 second timespan of the simulation, because the coefficient has a low value.

All in all the front widths show different behaviour dependent on the conditions set for the cases. Changing the Schmidt number poses a significant change within the results as showed and discussed. The main influence is the diffusion coefficient that has an effect on

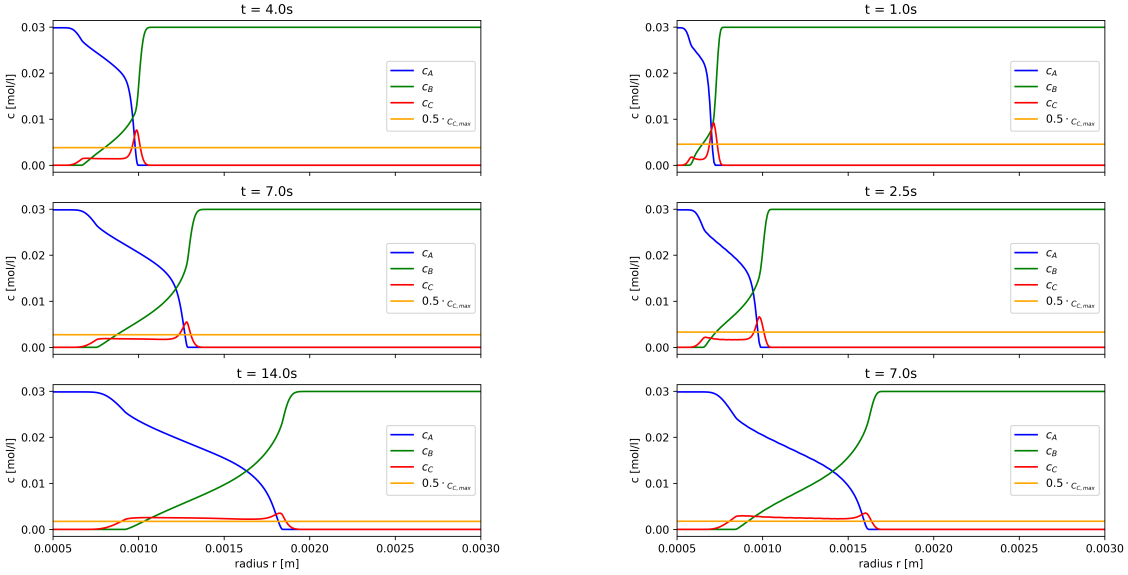

(a) h = 0.6mm case

(b) h = 0.4mm case

Figure 4.14.: Concentration plots for Pe = 931 Sc = 12000

where and when the front's width growth starts to happen. The Peclet number seems to mostly influence the width's maximum peak value but doesn't change the general behaviour of the front. That is the case, because the Peclet number mostly influences the input velocity, which influences the distortion of the front.

4.3. Formed Product

Within this section the total product formed is investigated.
For the case with a gap height of 0.2mm the total product formed starts with a linear growth which then slowly decays for all cases with a Schmidt number of 12000. The difference when lowering the Schmidt number, is that the initial production rate is higher and the decay starts earlier. In addition to the plot of the product C in mol against time in seconds, a linear fit is done with the data of the last 10 seconds. The fit approach is

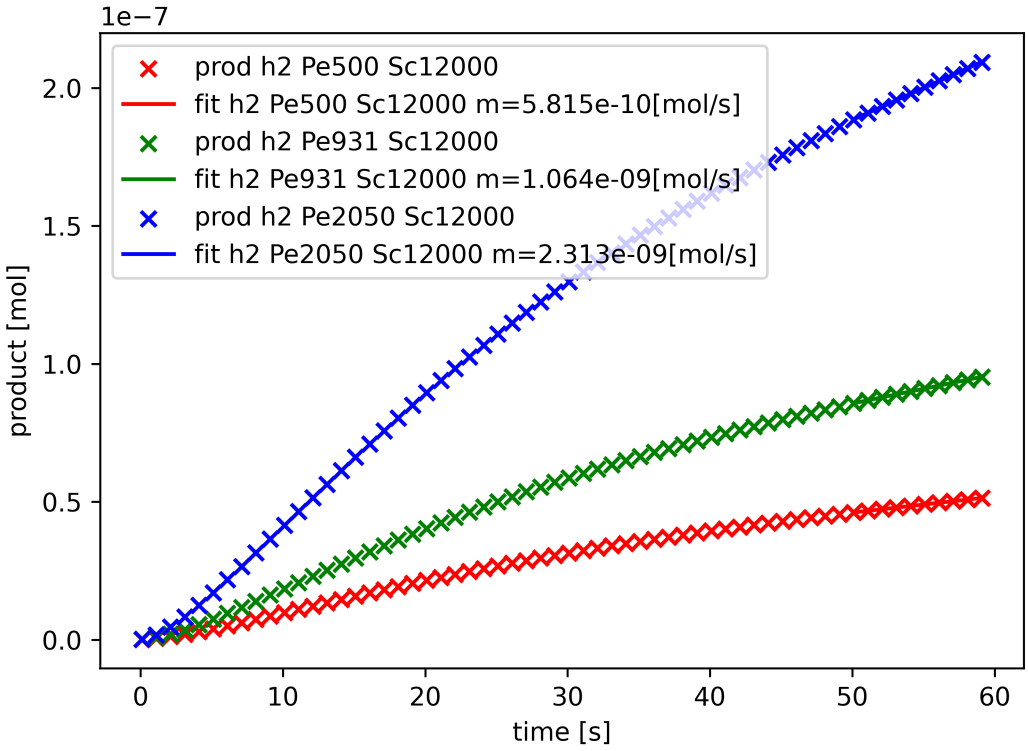

Figure 4.15.: Total amount of product for h = 0.2mm Sc = 12000

shown in Equation 4.2.

$$n_C\,[\text{mol}] = m\left[\frac{\text{mol}}{\text{s}}\right] \cdot t\,[s] + b\,[mol] \tag{4.2}$$

Since only the production rate m is of interest, only it's values are included in the diagrams.

The curve's shapes can be explained by looking at the influence of advection and diffusion. For the higher Schmidt number of 12000 the production rate only slightly lowers over the 60 seconds of simulation time. At the start of the simulation the front's shape is very narrow. The reactants A and B need to travel via diffusion through the front to form the product C. Since the diffusion coefficient is low the reaction rate in the beginning is also quite low. With time passing the fronts width gets wider and the distance the reactants have to travel grows. That is why the production rate decreases. The final value it reaches is dependant on the equilibrium that is build between the dif-

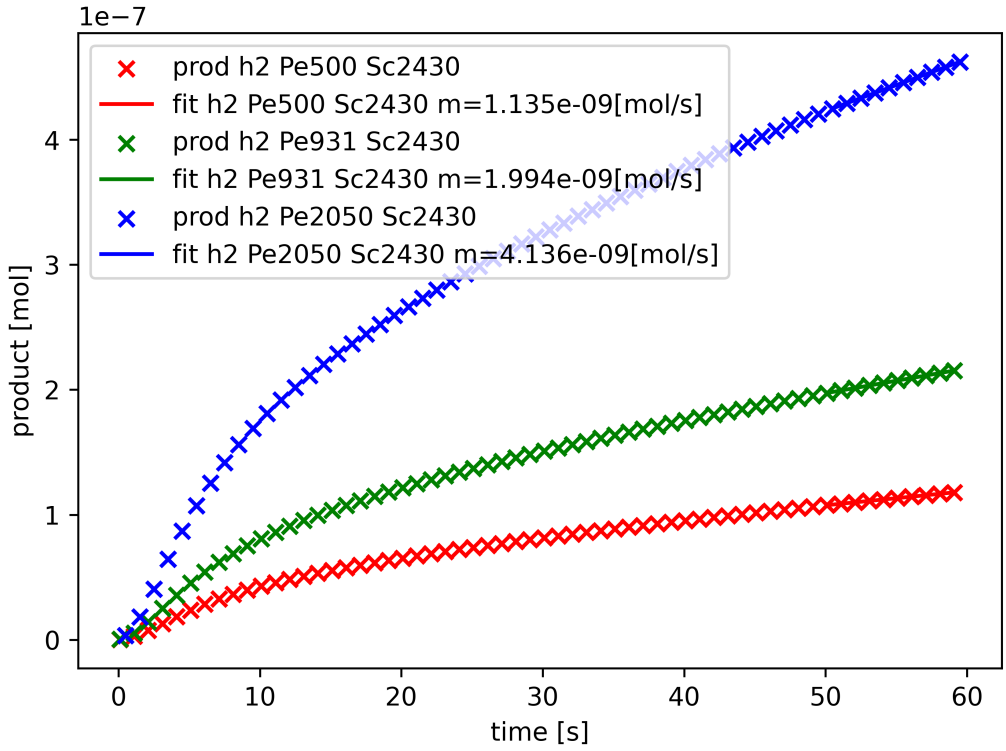

Figure 4.16.: Total product for h = 0.2mm Sc = 2430

fusion and the reaction process. With higher Peclet numbers the fronts distortion gets higher so new surface area is generated for the reaction to take place. That is a reason why the reaction rate is higher for higher Peclet numbers. The same arguments can be used to explain, why the initial production rate is high and then decreases for the cases with a Schmidt number of 2340. The higher diffusion coefficient in combination with the narrow front lead to this high production rate. The production rate at the end of the simulation is also affected by this showing nearly twice as high values for the lower Schmidt number cases of Figure 4.15 compared against the higher Schmidt number ones of Figure 4.16.

The total amount of product behaves very similar for the gap height of 0.4mm and 0.6mm. For that reason only the 0.4mm cases are analysed here. The results for the 0.6mm cases can be found in Section A.4. For the higher Schmidt number cases the total amount of product grows slowly in the first few seconds, but then increases linearly until

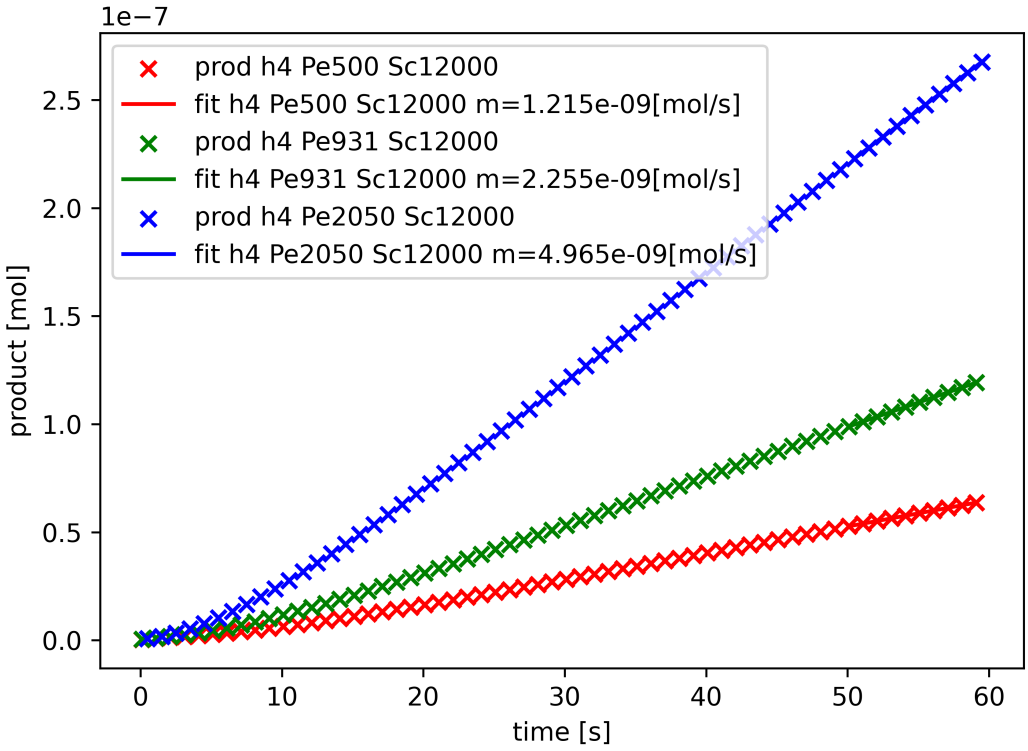

Figure 4.17.: Total product for h = 0.4mm Sc = 12000

the end for all cases. The production rate reached at the end is higher for higher Peclet numbers.

For the lower Schmidt number the graphs look very similar when comparing Figure 4.18 and Figure 4.16. The values are higher for the 0.4mm case, but that is a result of the higher gap height and therefore higher volumetric flow through the reactor.

The amount of product created is highly influenced by the Peclet number. With approximately doubling the Peclet number between different cases for the same Schmidt number, the total product produced at 60 seconds goes up by a bit more than a factor of 2. That can be seen when comparing the cases for all different gap heights. That results are directly linked to the different input velocities that can be taken from Table 3.9.

The cases with a gap height of 0.6mm and a Schmidt number of 12000 are still in the phase of higher production rate throughout the hole simulation run. In Figure 4.19 the front shapes are shown for a time of 60 seconds for both Schmidt numbers. From the image showing the higher Schmidt number case it can be seen that the front is still

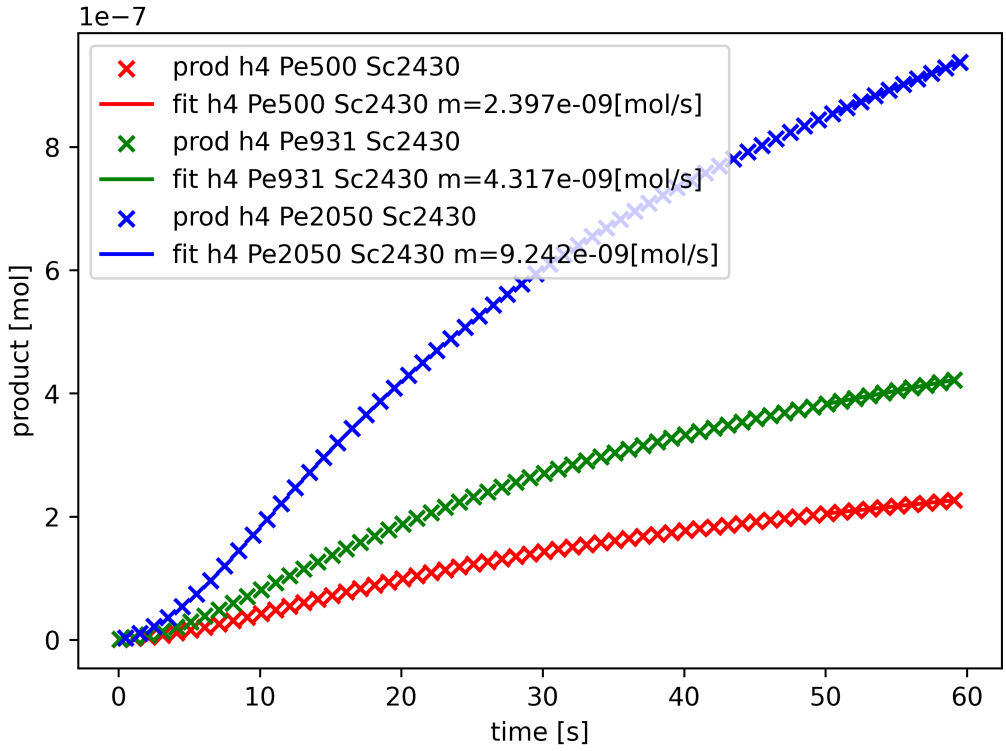

Figure 4.18.: Total product for h = 0.4mm Sc = 2430

building over the hole gap height, so the reaction rate would remain high until that is accomplished. A initial high production rate that after a while decreases can also be seen in the theoretical model developed by [24]. Comparing to their work, the cases for the high Schmidt number and a gap height of 0.4mm and 0.6mm seem to be in the proposed early time regime [24]. Comparing that to the lower Schmidt number case were the front has nearly reached its final form, only a slight decay is visible towards the end of the simulation. To get clearer evidence on when the production rate has reached its final constant value the simulations need to be run for longer durations.
In Table 4.1 all rates calculated by the linear fitting operation are shown.
The production rate shows a similar behaviour on a principle level within all investigated reactor geometries. The stages the fronts pass through in the 60 second time span of the simulation are different for the different gap heights.

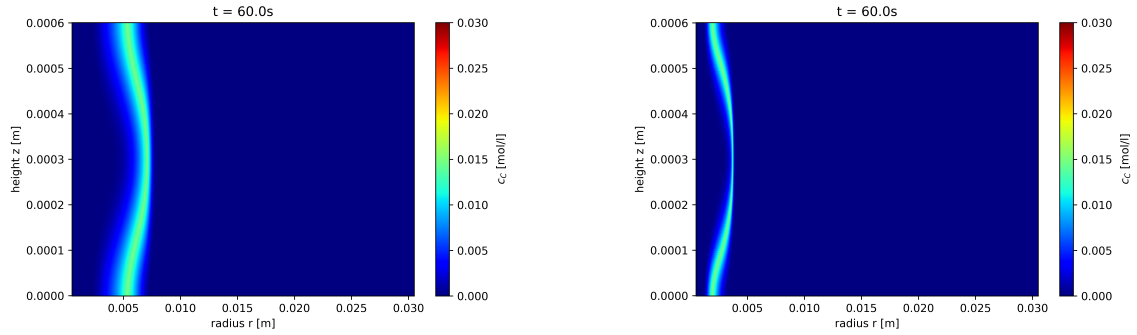

(a) Sc=2430 (b) Sc=12000

Figure 4.19.: Product concentration fields at t = 60s for h = 0.6mm Pe = 931

Table 4.1.: Production rates for all cases from linear fit

gap height [mm]	Pe	Sc	m [mol/s]
0.2	500	12000	5.815e-10
0.2	931	12000	1.064e-09
0.2	2050	12000	2.313e-09
0.2	500	2430	1.135e-09
0.2	931	2430	1.994e-09
0.2	2050	2430	4.136e-09
0.4	500	12000	1.215e-10
0.4	931	12000	2.255e-09
0.4	2050	12000	4.965e-09
0.4	500	2430	2.397e-09
0.4	931	2430	4.317e-09
0.4	2050	2430	9.242e-09
0.6	500	12000	1.196e-09
0.6	931	12000	2.246e-09
0.6	2050	12000	4.988e-09
0.6	500	2430	4.551e-09
0.6	931	2430	8.452e-09
0.6	2050	2430	1.874e-08

5. Discussion

All numerical investigations do have some limitations. Assumptions that are made and simplification that have been done do set boundaries. The limitations are discussed in this section.

The first limitation is, that the model is simulating a 2D case. The assumption has been made, that all cases show axisymmetric behaviour so only a 2D slice of the reactor is modelled. In the real world there are always some 3D effects, changing the front's behaviour compared to the simulation model. One of these effects could be mass transfer in tangential direction. Adding to the axisymmetric assumption, the homogenous velocity profile set as the inlet's boundary condition is impossible to meet in a real world experiment. Since in every Hele-Shaw cell the fluid injected has to come from somewhere, the velocity at the inlet is not homogeneous in it's magnitude and direction. This poses a large influence on the front's distortion at early times.

Other influences that can be observed under real world conditions, are different thermophysical properties of the species taking part in the reaction. Since two reactant molecules form one molecule of product they all have to have different densities, viscosities and diffusion coefficients. Within the model the reaction speed can be set to a very high value, but under normal conditions the reaction speed might have a lower value. The more crucial part, when looking at the reaction is, that there is no backwards reaction. Real world reaction systems always consist of a forward and backward reaction. The reaction could also have an impact on the temperature, lowering it in case of an endotherm one or raising it if it is an exothermal one. In addition to the reaction changing the temperature the reactants themself induce thermal mass into the system, affecting the temperature.

Within the model the influence of gravity can be turned of completely. Under normal conditions the gravitational effects can only be lowered but not get rid off. The only way to achieve 0g conditions in real world would be to do experiments at Lagrange points in space, like the one the James-Webb-Telescope is located at. Since that is not practically viable there will always be gravitational influences. With gravity always being there in the real world, the fronts might change in shape, due to density differences, as schematically shown in Figure 1.3.

In addition to the different thermophysical properties, the initial concentrations do influ-

ence especially the amount of product build. The influence of the ratio of the reactant's concentrations was investigated in [24] and shows an influence on all front metrics.
The front positions are mainly influenced by the Peclet number. Even higher Peclet numbers will probably do not result in a changing behaviour, if laminar conditions are still met.
The front width is influenced by Peclet and Schmidt number. Running the simulations for longer durations might answer the question, if the long-term regime of constant width is met or if something else changes at way later times. Most interest is here in the cases with the higher gap widths. The formed product shows the most interesting behaviour for the small Schmidt number. Lowering the Schmidt number even more might see an even bigger change in production rate.

6. Conclusion and Outlook

In this work a numerical study was performed for the reaction of $A + B \rightarrow C$ within a radial reactor. The numerical model was implemented using the software `ANSYS FLUENT`. Different geometries and conditions were investigated regarding the evolving front's shape, width and amount of product formed. The model validation was performed successfully using existing experimental data. The implementation and post processing is setup in a way that can easily be modified for the existing geometry or be applied to other models created in `ANSYS FLUENT` that are similar to the one used in this work. The model delivers more insight into the phenomenon of reaction-diffusion-advection fronts and provides information otherwise not accessible to experimental setups by giving a cross section view of the reactor. The change in reactor gap height has no significant influence on the front positions since the results for all geometries show similar behaviour. The front widths do show different behaviour under different gap heights. For the Schmidt number of 12000 all cases behave similarly with a fast initial growth trending towards a final constant value. The cases with a lower Schmidt number of 2430 do show significant changes for different reactor geometries. The visible peak in all plots do shift in position and sharpness. The total amount of product formed shows comparable results for all geometries. An early growth in product is followed by a decline towards a constant production rate. This production rate is mainly influenced by the Peclet number. For the highest gap height the production rate seems to mainly be inside the initial growing phase. For the lower gap heights the production rate declines at the end showing that the rate is in the process of transitioning towards the long-term constant value. The raw data generated by the simulation certainly do hide more valuable information. Further analysis could be done to the front's shape as done in [30, 31]. In addition to the already performed cases, that do have the some inlet concentrations for species A and B, the concentration ratio might be an interesting topic to look further into or the inlet's conditions could be varied in time. There are still more influences that might prove valuable to investigate in the future. The possibility of running cases in parallel could help reduce the amount of experiments needed in the future. The model could also be used for validating existing experimental runs with different conditions as long as the current limitations are thought of. Since experiments under 0g conditions are monetary expensive and consume a lot of time for preparation the developed model

provides a resource efficient alternative.
The developed model sets a step in the direction to gain further understanding on what is happening at the front's formation process at early time stages under 0g conditions. A foundation is laid in this work that can be used for further research and investigations.

A. Appendix

A.1. Mesh dependency

In Figure A.1 and Figure A.2 the mesh dependency studies for the cases with a gap height of 0.2mm and 0.6mm are shown.

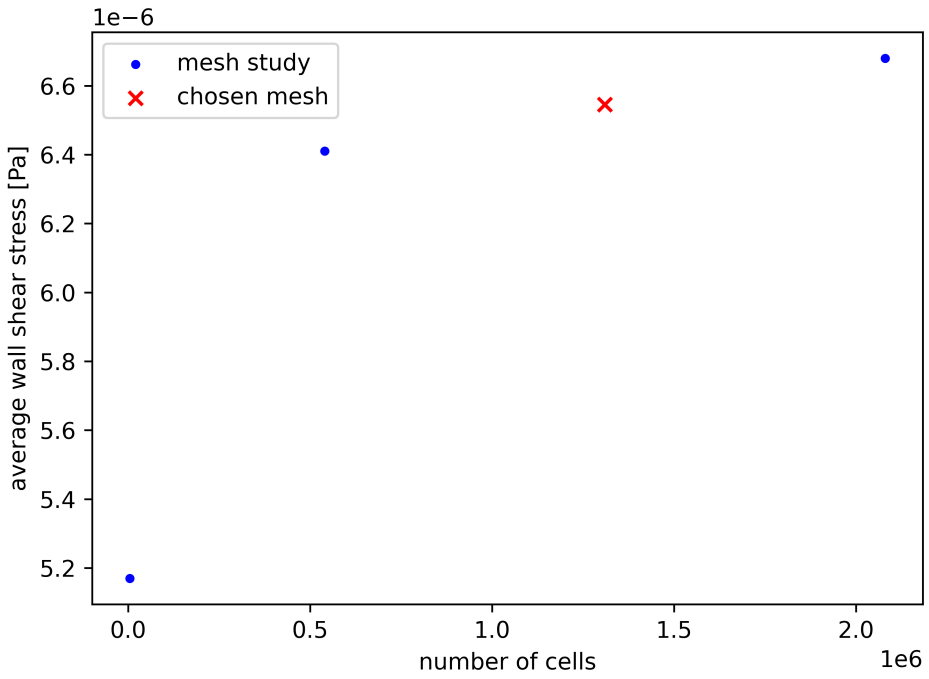

Figure A.1.: Mesh dependency study for geometry with 0.2mm gap height

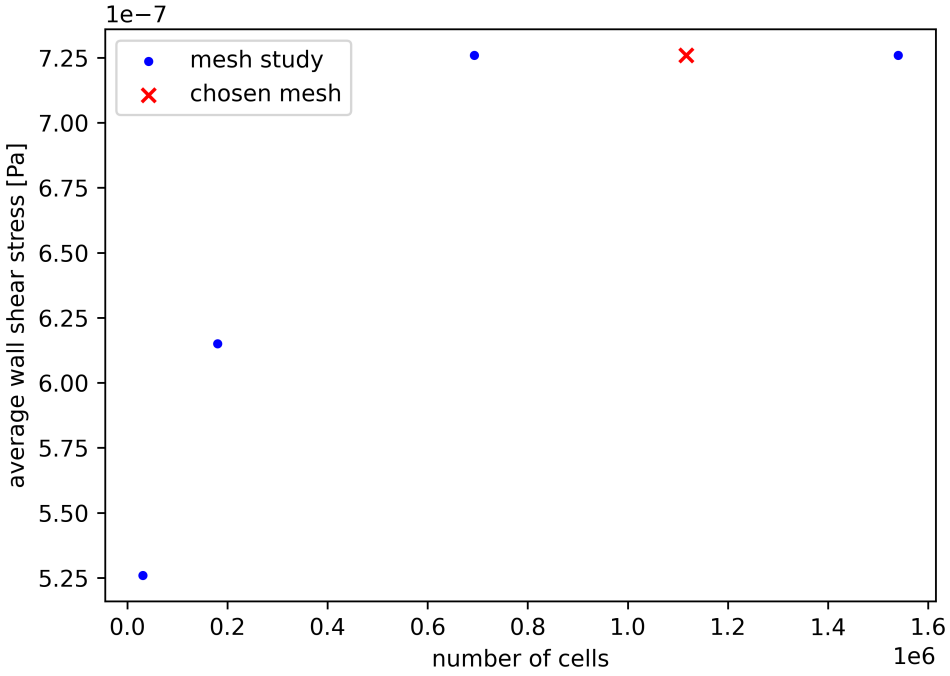

Figure A.2.: Mesh dependency study for geometry with 0.6mm gap height

A.2. Model implementation

In this part the model implementation and execution is explained.
When having to run a model for a variety of sets of input values it is useful to think about reducing the manual performed steps to a minimum. This has the advantages to provide a scalable solution if the set of input variables increases or the number of different values that need to be looked at grows. When having to set large amount of variables at different places within the model manually, the process is prone to errors that might not be detected until the results are computed or in case of small ones are not detected at all.
In general the developed solution follows the guideline shown in Figure A.3.
The first step that needs to be done when creating a set of cases is the creation of a base model. This step mostly includes the geometry creation and meshing. It is important that the results exported, that are directly influenced by the mesh are able to be further processed. That is why the mesh in this work's base models mostly consists out of squares and rectangles. The creation of the base model is done using the tool `ANSYS`

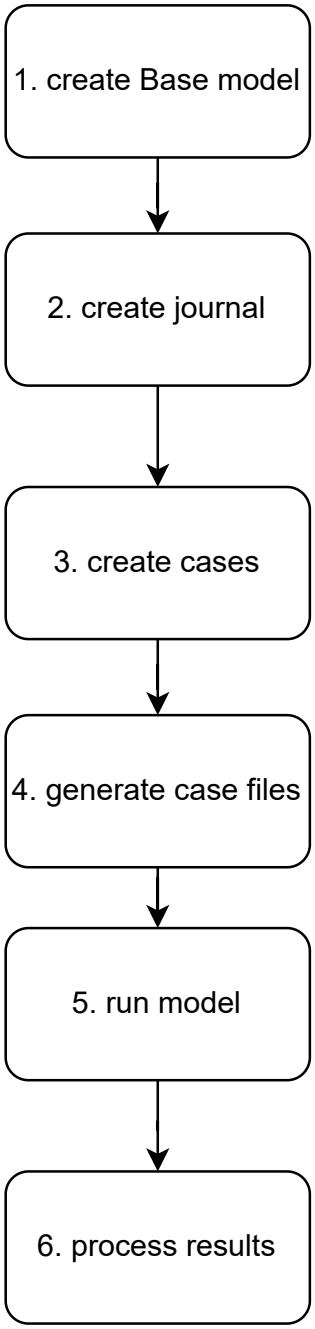

Figure A.3.: Implementation guideline

WORKBENCH.

The next step is to create a journal that sets all the values for the input variables. The file is called journal according to [26] and is used to automate ANSYS FLUENT model execution. This journal can easily be created by using the build in macro recording tool of ANSYS FLUENT. Within this journal all needed settings that are not already set within the base model itself must be included. A part of such a journal is shown in Listing A.1. One of the last steps of such a journal is the export of a model and a data file to a target location chosen by the user. This step is needed when looking into parallel execution of models that will be explained later.

Listing A.1: Journal example

```
...
; Set inlet velocity
(cx-gui-do cx-set-expression-entry " ... (Velocity Magnitude)" '("%input_vel%" . 0))
(cx-gui-do cx-activate-tab-index "Velocity Inlet*Frame2*Frame2" 3)
; Set minimum/maximum timestep size
(cx-gui-do cx-activate-item "Run Calculation*Table1*Table7(Time
    Advancement)*Table3(Parameters)*Table6*Table1*PushButton1(Settings)")
(cx-gui-do cx-set-real-entry-list "... (Minimum Time Step Size)" '( %timestep_min%))
(cx-gui-do cx-set-real-entry-list "... (Maximum Time Step Size)" '( %data_export_interval%))
(cx-gui-do cx-activate-item "Adaptive Time Stepping*PanelButtons*PushButton1(OK)")
...
; Export Case & Data
(cx-gui-do cx-activate-item "MenuBar*WriteSubMenu*Case & Data...")
(cx-gui-do cx-set-file-dialog-entries "Select File" '( %case_export_path%) "CFF Case/Data
    Files (*.cas.h5 *.dat.h5 )")
```

From the highlighted lines in Listing A.1 it can be seen that for each variable that needs to be set by the journal a variable name is defined and put between to two % signs for easier identification. With this approach new variables can be efficiently added. When the journal is created by the user and the journal functionality is tested and proven the cases need to be created. A case is defined here as one model execution with a set of input parameters and their values. The cases can be created in different ways but need to be provided in .json format in the end. An example of such a case in correct format can be seen in Listing A.2. The file providing the cases can contain as many as needed.

Listing A.2: case example

```
{
    "h2r3_P346E2_S122E3": {
        "export_times": "flow_time",
        "total_time": 360.0,
        "fixed_timesteps": 1,
```

```
        "timestep_min": 0.001,
        "data_export_interval": 1.0,
        "input_vel": 0.00142206,
        "inlet_xA": 0.00054,
        "init_phiB": 0.003,
        "viscosity": 1e-06,
        "diffusion": 8.22e-10,
        "iterations": 30,
        "queue": "milan",
        "tasks_p_node": 32,
        "wall_time": "96:00:00",
        "post_wall_time": "48:00:00",
        "case": "h2_r3_6e-6.cas.gz"
    }
}
```

After the cases are provided and all previous steps are done as well all cases can be created by running the developed tool `journal.py`. This tool creates a folder for each case at the destination provided within `conf.json` and creates all files needed to execute the case. This script needs to be run on a machine that has `ANSYS FLUENT` installed and is able to write to the desired destination. The version used here is `Fluent 2022 R1`. Having all files needed for case execution within the case's folder makes parallel case execution possible because cases have no cross referenced files. That also helps with developing, debugging and checking the case at future times, as all things necessary are there.

If all cases are created successfully they can be run in parallel on an High Performance Computing (HPC) Cluster. The journal template files developed within this work also provide a variant for local execution but that is not recommended when having a large amount of cases to run and if the number of cells get rather high. Since a HPC Cluster was used here this work focuses on that execution variant.

A brief overview of the Cluster used is provided in Figure A.4 [32]. A Cluster usually consists of 5 different components. To provide a high amount of computational power compute nodes are needed. This can be as many as rack space and or other limiting factors are available. To feed the compute nodes with calculations to perform the head nodes are doing the load balancing. A task that needs to be performed on the cluster is called job. These jobs are created on the login nodes and then submitted to the head nodes that run a queueing system. The one used here is `slurm`. For data and storage access all nodes are connected to a storage server using an industry standard high capacity network connection. It is not wise to run the login and head nodes on the same piece of hardware as one could think because if the head nodes crash the hole

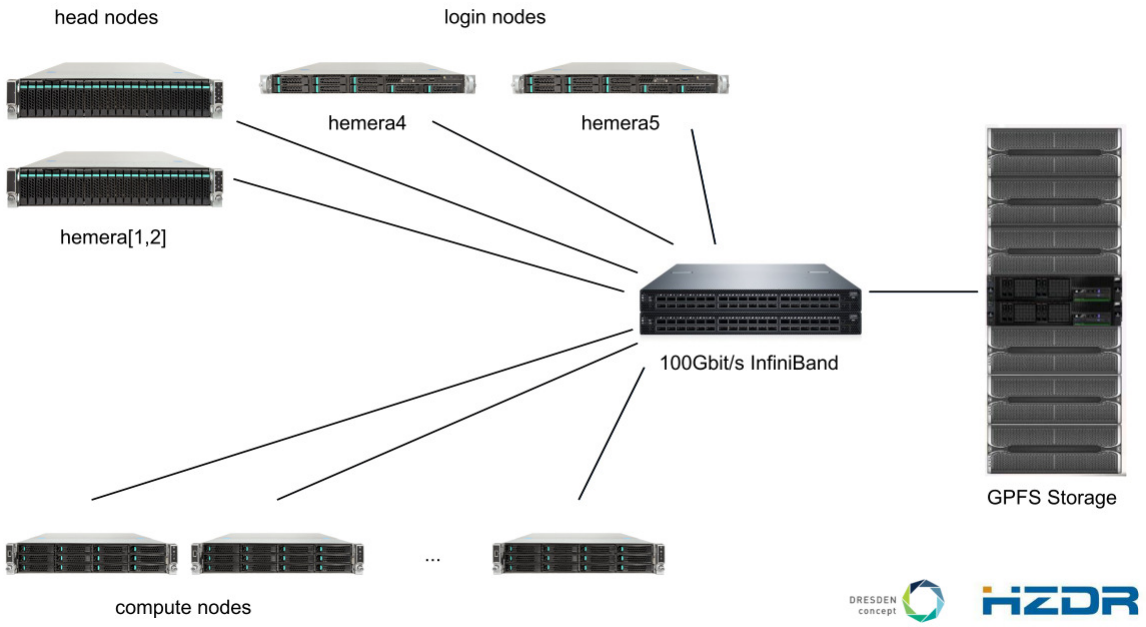

Figure A.4.: HPC Cluster Overview

cluster becomes inoperable. To minimise this risk these two tasks are separated onto different machines.

For the queueing system `slurm` to accept a job a few parameters need to be set. Each job needs to have a partition and wall time set. The partition refers to a given queue on the cluster. There are different queues for different purposes and not all of them are available to each user. The wall time is needed to set the maximum time a job is allowed to run. This prevents failing jobs to block the cluster for an infinite time. In addition to these two parameters, as shown in Listing A.2 the hardware requirements of a job need to be set. This is the amount of nodes the job needs and the amount of CPUs that are reserved on each node. Since `ANSYS FLUENT` calculations can not be distributed over more than one node the amount of nodes is always 1. The CPU Cores used can be in a range of 1 to the maximum the hardware bound to the chosen queue has to offer. Higher demand of resources in combination with long wall times might lead to high queueing times so it is worth spending a thought on them. When having cluster access the developed script `run.sh` can be run with the option `-a` to run all jobs that have not generated any data. After some time has passed the script `time_estat.py` can be run to get a estimation of the remaining job runtime using Equation A.1. The script will also warn the user if the set wall time is lower than the estimated execution time.

The tool grabs the current job execution status out of the simulation's log file and uses the current job run time to calculate the total and remaining execution time.

$$t_{exec,remain} = \underbrace{\frac{t_{sim,total}}{t_{sim,current}} \cdot t_{exec,current}}_{\text{total execution time}} - t_{exec,current} \tag{A.1}$$

These values can be easily compared with the set wall time.

A.3. Front positions

Here you can see the front position plots for the cases with a gap height of 0.4mm in Figure A.6 and Figure A.5 and 0.6mm in Figure A.7 and Figure A.8.

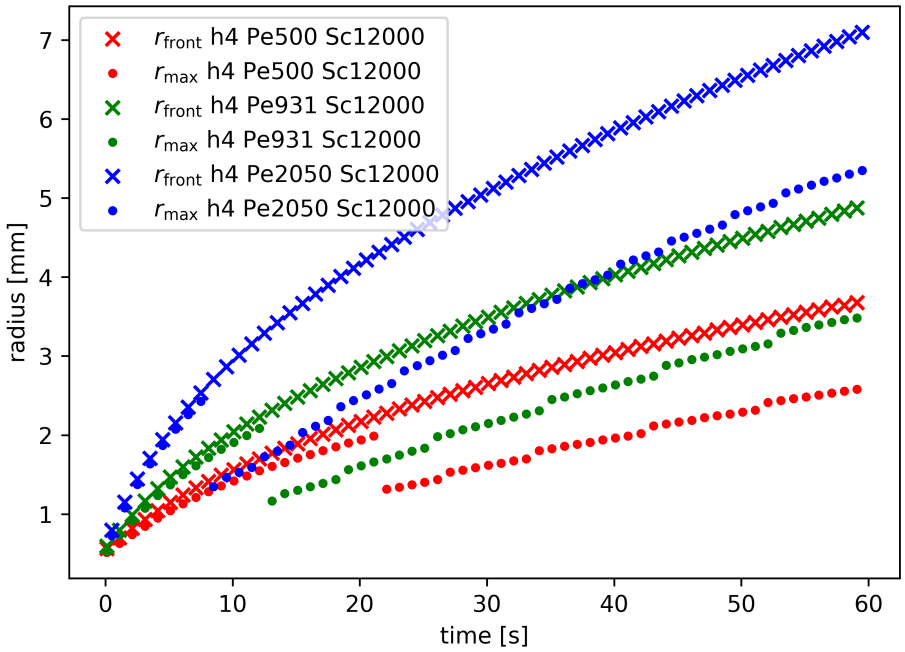

Figure A.5.: Front positions for h = 0.4mm Sc = 12000

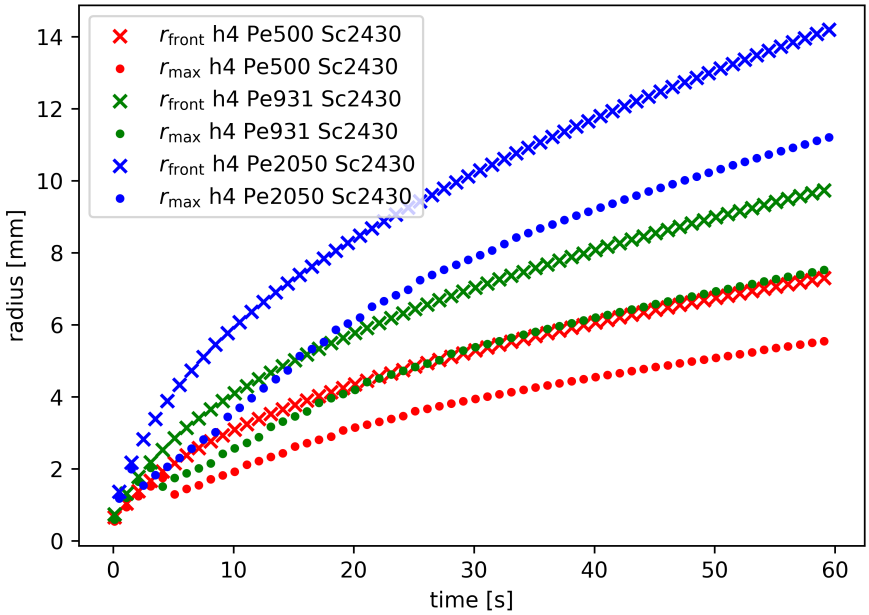

Figure A.6.: Front positions for h = 0.4mm Sc = 2430

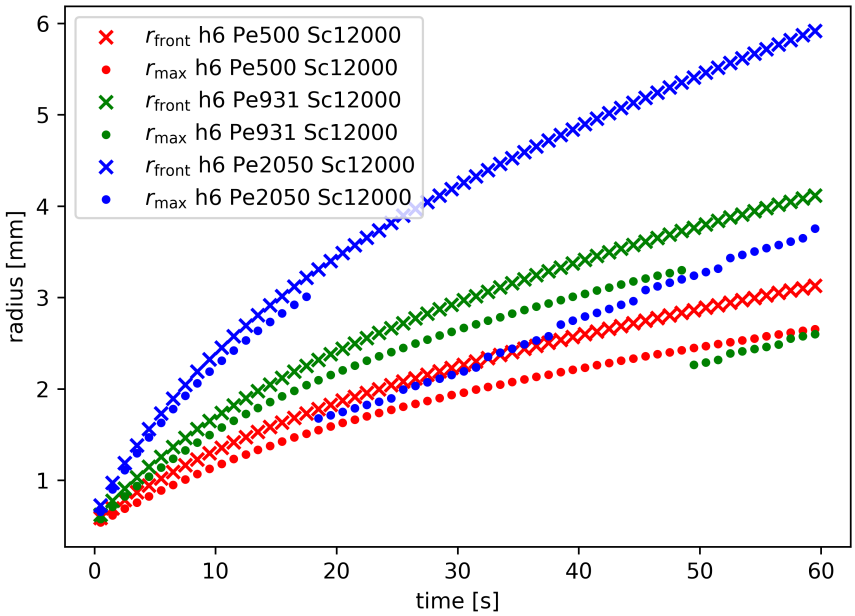

Figure A.7.: Front positions for h = 0.6mm Sc = 12000

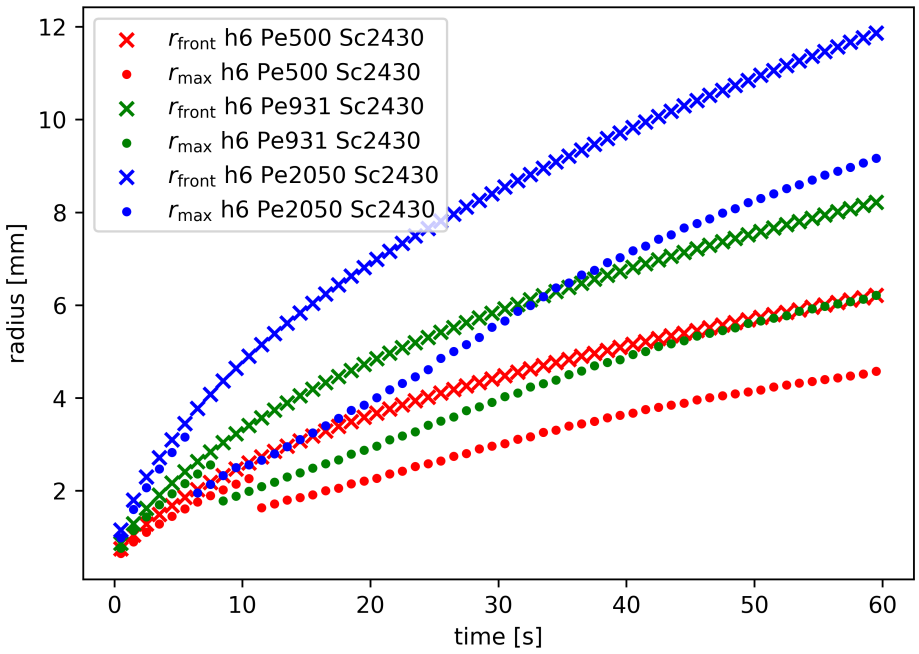

Figure A.8.: Front positions for h = 0.6mm Sc = 2430

A.4. Production rate

Here the plots of the production rate for the cases with a gap height of 0.6mm are shown in Figure A.9 for a Schmidt number of 12000 and in Figure A.10 for a Schmidt number of 2430.

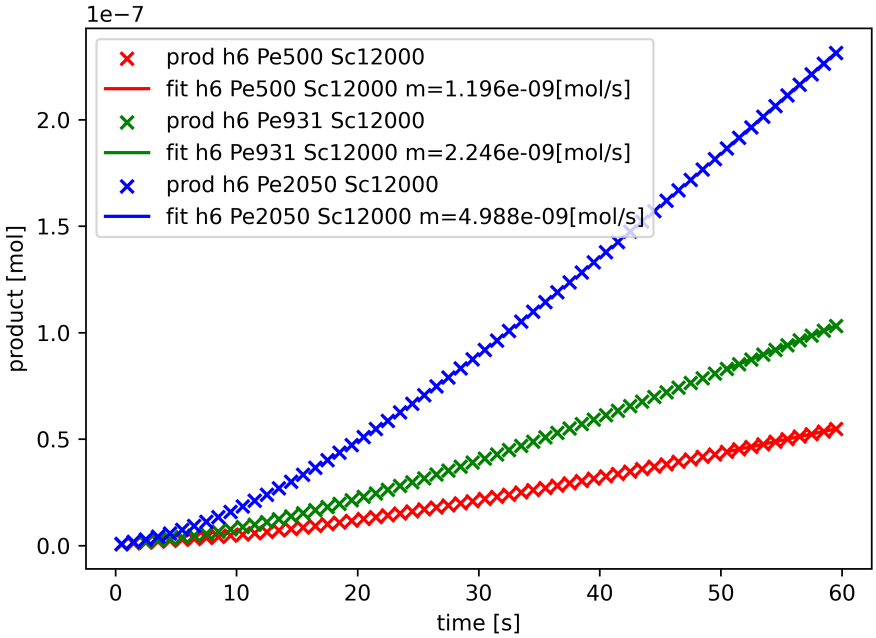

Figure A.9.: Total product for h = 0.6mm Sc = 12000

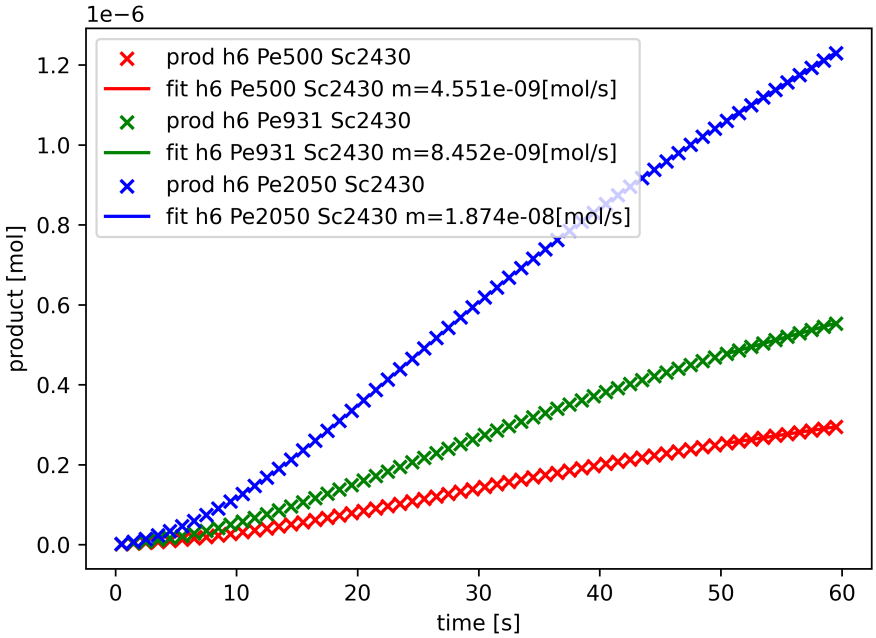

Figure A.10.: Total product for h = 0.6mm Sc = 2430

A.5. Errors

Here the errors are explained in greater detail. The models solution is an iterative procedure as described in section 2.4. Within this process the solution obtained within one iteration is used as initial starting point for the next one. The procedure also involves a correction step as shown for the pressure and velocity field in Figure 2.5. These corrections can be tracked over the iterations done throughout the simulation run. The results also called `residuals` can be seen in Figure A.11. To check that

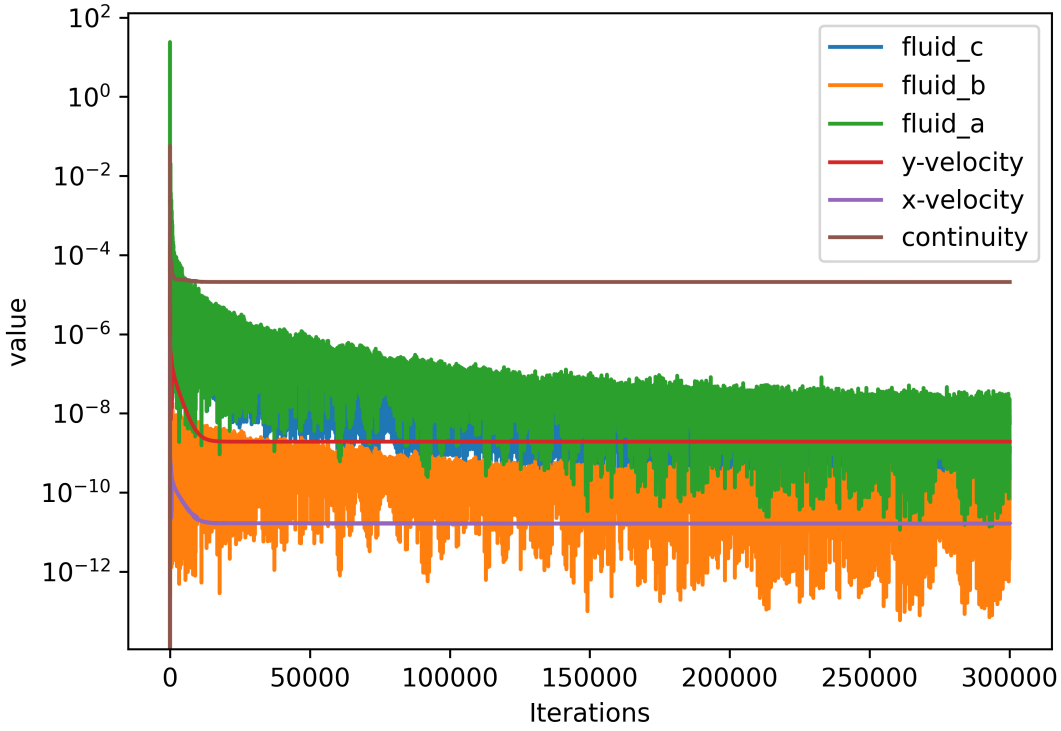

Figure A.11.: Example residuals plot

the model has converged for a solution step thresholds for the residuals are set. If the residual value for a variable is below the set threshold the solution has converged and the next step is performed. From the plot it can be seen that the residuals do have values of 10^{-5} and below so the model performs well for the given example. The values do jump up and down a bit for certain variables that is due to the moving flow and changing fluid composition resulting from the reaction. For the continuity and velocity variables the residuals are represented by a straight line because once the velocity field

is established it does not change any more.
The residuals give an indication on the model's errors and can be used as well to check if the model behaves correctly or which part has to be changed if the solution does not converge or other errors occur.

Bibliography

[1] Corning AFR. Advanced flow reactors. `https://www.corning.com/media/worldwide/Innovation/documents/G1_WEB.pdf`. Accessed: 2022-12-28.

[2] Yorgos Stergiou, Marcus JB Hauser, Alessandro Comolli, Anne Brau, Fabian and, Gábor Schuszter, Paszkál Papp, Dezső Horváth, Clément Roux, Véronique Pimienta, et al. Effects of gravity modulation on the dynamics of a radial a+ b→ c reaction front. *Chemical Engineering Science*, 257:117703, 2022.

[3] Octave Levenspiel. *Chemical reaction engineering*. John wiley & sons, 1998.

[4] Shanshan Chen, Yuan Lou, and Junjie Wei. Hopf bifurcation in a delayed reaction–diffusion–advection population model. *Journal of Differential Equations*, 264(8):5333–5359, 2018.

[5] Yan Wang and Junping Shi. Persistence and extinction of population in reaction-diffusion-advection model with weak allee effect growth. *SIAM Journal on Applied Mathematics*, 79(4):1293–1313, 2019.

[6] Kousuke Kuto, Hiroshi Matsuzawa, and Rui Peng. Concentration profile of endemic equilibrium of a reaction–diffusion–advection sis epidemic model. *Calculus of Variations and Partial Differential Equations*, 56(4):1–28, 2017.

[7] Julia V Noble. Geographic and temporal development of plagues. *Nature*, 250(5469):726–729, 1974.

[8] Robert M May. *Infectious diseases of humans: dynamics and control*. Oxford University Press, 1991.

[9] Toshiyuki Nakagaki, Hiroyasu Yamada, and Masami Ito. Reaction–diffusion–advection model for pattern formation of rhythmic contraction in a giant amoeboid cell of thephysarumplasmodium. *Journal of theoretical biology*, 197(4):497–506, 1999.

[10] Ute Ebert and Wim van Saarloos. Front propagation into unstable states: universal algebraic convergence towards uniformly translating pulled fronts. *Physica D: Nonlinear Phenomena*, 146(1-4):1–99, 2000.

[11] Iacopo Mastromatteo, Bence Toth, and J-P Bouchaud. Anomalous impact in reaction-diffusion financial models. *Physical review letters*, 113(26):268701, 2014.

[12] Daniel M Abrams and Steven H Strogatz. Modelling the dynamics of language death. *Nature*, 424(6951):900–900, 2003.

[13] Fabian Brau and Anne De Wit. Influence of rectilinear vs radial advection on the yield of a+ b→ c reaction fronts: A comparison. *The Journal of chemical physics*, 152(5):054716, 2020.

[14] Barbara Heidel, Charles M Knobler, Rudolph Hilfer, and Robijn Bruinsma. Pattern formation at liquid interfaces. *Physical review letters*, 60(24):2492, 1988.

[15] Alexandra von Kameke, Florian Huhn, Alberto P Muñuzuri, and Vicente Pérez-Muñuzuri. Measurement of large spiral and target waves in chemical reaction-diffusion-advection systems: Turbulent diffusion enhances pattern formation. *Physical review letters*, 110(8):088302, 2013.

[16] Gaábor Schuszter, Fabian Brau, and Anne De Wit. Calcium carbonate mineralization in a confined geometry. *Environmental Science & Technology Letters*, 3(4):156–159, 2016.

[17] Kinko Tsuji and Stefan C Müller. Chemical reaction evolving on a droplet. *The journal of physical chemistry letters*, 3(8):977–980, 2012.

[18] Mazen Al-Ghoul and Rabih Sultan. Simulation of geochemical banding: Theoretical modeling and fractal structure in acidization-diffusion-precipitation dynamics. *Physical Review E*, 100(5):052214, 2019.

[19] L Gálfi and Z Rácz. Properties of the reaction front in an a+ b→ c type reaction-diffusion process. *Physical Review A*, 38(6):3151, 1988.

[20] Z Jiang and C Ebner. Simulation study of reaction fronts. *Physical Review A*, 42(12):7483, 1990.

[21] Yong Eun Lee Koo and Raoul Kopelman. Space-and time-resolved diffusion-limited binary reaction kinetics in capillaries: experimental observation of segregation, anomalous exponents, and depletion zone. *Journal of Statistical Physics*, 65:893–918, 1991.

[22] Kerstin Eckert, Laurence Rongy, and Anne De Wit. A+ b→ c reaction fronts in hele-shaw cells under modulated gravitational acceleration. *Physical Chemistry Chemical Physics*, 14(20):7337–7345, 2012.

[23] Ágota Tóth, Gábor Schuszter, Nirmali Prabha Das, Emese Lantos, Dezső Horváth, Anne De Wit, and Fabian Brau. Effects of radial injection and solution thickness on the confined a+ b→ c chemical fronts. *Physical Chemistry Chemical Physics*, 22(18):10278–10285, 2020.

[24] Alessandro Comolli, Anne De Wit, and Fabian Brau. Dynamics of a+ b→ c reaction fronts under radial advection in a poiseuille flow. *Physical Review E*, 104(4):044206, 2021.

[25] Hyundong Kim, Ana Yun, Sungha Yoon, Chaeyoung Lee, Jintae Park, and Junseok Kim. Pattern formation in reaction–diffusion systems on evolving surfaces. *Computers & Mathematics with Applications*, 80(9):2019–2028, 2020.

[26] UDF Manual. Ansys fluent 12.0. *Theory Guide*, 2009.

[27] Henk Kaarle Versteeg and Weeratunge Malalasekera. *An introduction to computational fluid dynamics: the finite volume method*. Pearson education, 2007.

[28] Marwan Darwish and Fadl Moukalled. *The finite volume method in computational fluid dynamics: an advanced introduction with OpenFOAM® and Matlab®*. Springer, 2021.

[29] Rutherford Aris. On the dispersion of a solute in a fluid flowing through a tube. *Proceedings of the Royal Society of London. Series A. Mathematical and Physical Sciences*, 235(1200):67–77, 1956.

[30] Lazaro J Perez, Juan J Hidalgo, and Marco Dentz. Upscaling of mixing-limited bimolecular chemical reactions in poiseuille flow. *Water Resources Research*, 55(1):249–269, 2019.

[31] Emmanuel Villermaux. Mixing by porous media. *Comptes Rendus Mécanique*, 340(11-12):933–943, 2012.

[32] Dr. Hendrik Schulz. Hardware & numerics. `https://www.hzdr.de/db/Cms?pOid=67578`. Accessed: 2022-12-15.

Selbständigkeitserklärung

Ich versichere, dass ich die vorliegende Arbeit selbständig verfasst und keine anderen als die angegebenen Quellen und Hilfsmittel benutzt habe. Ich reiche sie erstmals als Prüfungsleistung ein. Mir ist bekannt, dass ein Betrugsversuch mit der Note "nicht ausreichend" (5,0) geahndet wird und im Wiederholungsfall zum Ausschluss von der Erbringung weiterer Prüfungsleistungen führen kann.

Name:

Vorname:

Matrikelnummer:

Dresden, den .....

Unterschrift